Open Ceramics 26 (2026) 100959

Contents lists available at ScienceDirect

Open Ceramics

journal homepage: www.sciencedirect.com/journal/open-ceramics

Investigation of the (thermo-)mechanical properties and the chemical resistance towards ammonia combustion atmosphere of alumina-based model structures manufactured via Fused Granulate Fabrication

Benjamin Bock-Seefeld [a,*], Daniel Kretzler [b], Claudia Heuer [a], Marc Neumann [a], Jana Hubálková [a], Björn Stelzner [b], Oliver T. Stein [b], Dimosthenis Trimis [b], Christos G. Aneziris [a], Nora Brachhold [a]

[a] *TU Bergakademie Freiberg, Institute of Ceramics, Refractories and Composite Materials, 09599 Freiberg, Germany*
[b] *Karlsruhe Institute of Technology, Engler-Bunte-Institute Combustion Technology, 76131 Karlsruhe, Germany*

ARTICLE INFO

Keywords:
Additive manufacturing
Fused granulate fabrication
Ammonia combustion
Thermal shock performance

ABSTRACT

This study focuses on the fabrication of alumina-based model samples by fused granulate fabrication for the application in burner components for ammonia combustion. Three compositions were investigated: Two alumina systems with different initial grain size (A1-tabular alumina, A2-reactive alumina) and alumina (AZT) with MgO-stabilized ZrO_2- and TiO_2-additions. Young's modulus and flexural strength were determined after sintering and after up to five thermal shocks. A1 exhibited the best suitability for repeated thermal shocks, followed by A3. The high interparticle porosity of A1 limited crack propagation and resulted in a slow, gradual loss in elastic modulus (maximum loss of 8.6%) and strength (maximum loss of 35.7%) with increasing number of thermal shocks. Microstructural features due to the additive manufacturing process could enhance thermal shock performance. The materials were tested in ammonia combustion atomosphere at approx. 1500 °C for 1 h and showed no phase alterations. Model components with application-near geometries were successfully realized.

1. Introduction

The generation of thermal energy for high-temperature applications by combustion processes demands devices and components, which have to be adjusted to the process conditions of the individual applications [1,2]. Typical aspects to be considered are service temperature, corrosive reactions due to contact with the specific fuel and formed gaseous products in the flame and the exhaust gas, abrasion due to gas streams as well as thermomechanical load due to temperature gradients during ignition and the switching-off of the device [2].

Ceramic materials are commonly applied in combustion processes because of their high melting point and hence, their high service temperature [2]. Numerous ceramic materials are applied as components in combustion devices for different applications, e.g. as material in porous burners [3], as lining material [4] but also as casing material [5].

According to the literature, numerous materials are used in combustion applications. On the one hand, single compound materials are applied such as alumina, silicon carbide and zirconia [3]. Chalia et al. summarize their main advantages and disadvantages as follows [3]: Alumina is characterized by a high chemical stability and a high application temperatures at a comparatively low price, but has a relatively low thermal conductivity and limited thermal shock resistance. Silicon carbide exhibits a high thermal conductivity accompanied by good thermal shock properties. Its silicon dioxide surface layer formed at elevated temperatures in presence of oxygen works as protective passivation but limits the maximum service temperature of the material [6]. Zirconia provides high service temperatures and high corrosion resistance. By adjusting the stabilizer content, the specific phase distribution of high temperature phases (tetragonal/cubic) and the monoclinic low temperature phase can be determined and used for tailored phase transformation under thermomechanical load to improve thermal shock resistance. However, zirconia-based materials are relatively cost intensive and sensitive to water containing environments where humidity favors the transformation to the monoclinic phase and thus the degradation of the material [3,7].

On the other hand, composite materials are interesting for

---

* Corresponding author.
E-mail address: benjamin.bock@ikfvw.tu-freiberg.de (B. Bock-Seefeld).

https://doi.org/10.1016/j.oceram.2026.100959
Received 2 March 2026; Received in revised form 27 March 2026; Accepted 30 March 2026

combustion applications, since the single material advantages can be combined and the disadvantages can be mitigated. Additionally, further additives can be added to improve the material properties. An example for such a combination of compounds is a layer-wise structure. For instance, Liang et al. [8] infiltrated a SiC-Al_2O_3-SiO_2 compound with an alumina-coating forming an alumina surface layer with a mullite-bonded SiC intermediate layer and alumina-filled cavities. This concept resulted in the formation of additional mullite as secondary phase and led to an improvement of the components' compressive strength and thermal shock performance. Furthermore, an alumina-based system is proposed, which contains small amounts of ZrO_2 and TiO_2 (each up to 2.5 wt%) and can be described by the phase diagram alumina-zirconia-titania (AZT). This material composition results in a multiphase material system of initial phases and newly formed secondary phases during sintering (e.g. Al_2TiO_5) [5,9,10]. The AZT material is characterized by a multiphase microstructure with differing thermal expansion coefficients for each phase, which are strongly anisotropic in case of Al_2TiO_5. Moreover, Al_2TiO_5 is metastable at temperatures below 1280 °C and can decompose under thermal load [11]. The decomposition is accompanied by a volume shrinkage, which causes compressive stresses in the surrounding alumina matrix. This partially compensates tensile stresses during thermal shock load and favors the thermal shock resistance of AZT material [12]. Furthermore, grain growth of alumina grains can take place due to the effect of titania as sintering aid [13]. Additionally, zirconia can be subjected to phase transformations, which are accompanied by volume changes. All these effects result in a crack formation in the microstructure of AZT material. This is very advantageous in terms of thermal shock resistance because of its ability to stop crack propagation and to dissipate crack energy.

Apart from the chemical composition, the grain size of the raw materials is of particular importance. Fine grained systems in the range of micrometers are used for filigree components such as porous components of burners [3,6]. Coarse grained systems with maximum grain sizes larger than one millimeter are used for bulk components, e.g. for lining applications, where the broad raw material grain size distribution permits the manufacturing of large-scale components with a sintering shrinkage close to 0 %. Furthermore, the resulting microstructure is favorable for a high thermal shock resistance [4].

Due to the evolution from fossil fuel-based processes to systems using renewable energy resources, alternative energy carriers come into focus [14]. Ammonia is such an alternative, which is intended to be employed for storage, transport and application of renewable energy in industrial processes [15]. Therefore, it is also considered as a future energy carrier for combustion. However, the direct use of ammonia in the combustion process is challenging due to its low reactivity combined with low flame speed making a stable combustion difficult [16]. A further problem is the emergence of relevant pollutant emissions (residual ammonia, nitrogen oxides) [17].

To address these issues, advanced burner concepts have been proposed, including the combustion of ammonia within porous inert media, where radiative, conductive and convective heat recirculation, along with tailored reaction zones, can support stable combustion of NH_3/air mixtures without external preheating or hydrogen addition [18,19]. Another promising concept is the non-premixed combustion of ammonia with air, which has been suggested to reduce NO_x emissions [20,21]. Combining both strategies, namely non-premixed operation and combustion within porous media, may offer further advantages by stabilizing the flame through enhanced heat recirculation while retaining the emission benefits of locally controlled mixing.

However, realizing non-premixed combustion inside within media imposes specific design and material requirements. Separate feeding channels for ammonia and air must be integrated into the porous structure to deliver reactants to the reaction zone while withstanding high temperatures, thermal shocks, and oxidizing or reducing environments [22].

In this context, both the number of channels and their geometric characteristics are expected to influence mixing, stabilization, and heat recirculation. Key geometric parameters include channel diameter, tortuosity, and length, as well as the spatial distribution of the channels and the possibility of graded properties. Consequently, these structures must be fabricated from ceramic materials and tailored in geometry and thermal properties to enable robust operation under ammonia combustion conditions.

This can be realized by sheet-gyroid structures providing two separate spaces with intertwined channel character. The generation of such structures by powder-based technology as it is typical for ceramic materials is not possible by conventional ceramic shaping technologies due to the 3-dimensional curved character of the intended structures [23,24].

For such complex geometries, additive manufacturing (AM) processes allow new possibilities of fabrication due to the layer-wise build-up process of the components [23]. There are three main additive manufacturing concepts [23]: powder bed-based technologies (e.g. selective laser sintering, binder jetting), suspension-based technologies (e.g. stereolithography, digital light processing) and extrusion-based technologies (e.g. fused filament fabrication (FFF), fused granulate fabrication (FGF)).

Generally, extrusion-based AM processes require feedstocks containing a multi-component binder system and ceramic particles as filler material (normally $\geq$ 50 vol %) [23,24]. The binder system has typically a thermoplastic behavior so that it can be extruded through a heated nozzle to build up the intended geometry in a layer-wise way. The FGF process has the advantages that no challenging filament production is necessary and waste material or defective parts from the printing process can easily be reused in the production of the granulates. After the printing process, the binder has to be removed in a debinding step, which can be based on different technologies (solvent-based debinding, wick-debinding, thermal debinding) [23]. Finally, the sintering step takes place causing the ceramic bonding between the particles and creating the intended ceramic component.

The manufacturing of components for high-temperature application by means of the FGF process allows the creation of a microstructure with a micro-porosity (up to 10 μm), which has a positive effect on the thermal shock performance [25–27]. Furthermore, internal macro-cavities with a size range of millimeters can fulfill lightweight construction requirements and promote thermal shock resistance [27].

The present study investigated potential alumina-based material systems for the application in ammonia combustion components due to the high refractoriness and chemical stability of Al_2O_3. Additive manufacturing based on FGF was conducted to use the positive effect of the resulting microstructure on the thermal shock performance of the components. Two pure alumina systems were investigated differing by their initial grain size. Furthermore, AZT with MgO-stabilized ZrO_2 and TiO_2 additions (2.5 wt % each) was considered. The AZT material was based on a well printable alumina raw material from previous investigations [24] with added MgO-stabilized ZrO_2 and TiO_2 according to former studies [12]. Model samples were fabricated by FGF followed by a pure thermal debinding [24] to realize the corresponding 3D-printed microstructure. The influence of the microstructure, the initial phase composition and the grain size on the thermomechanical properties of the three material systems was investigated in thermal shock tests under compressed air. Furthermore, the samples were exposed to ammonia combustion atmosphere at application-relevant temperatures to evaluate their chemical resistance using scanning electron microscopy equipped with energy dispersive x-ray spectroscopy (EDX) and electron backscatter diffraction (EBSD). Finally, model components were manufactured to test the whole process line with regard to application near geometries. The analyses within this study aimed at the identification of a suitable material system for the future manufacturing of tailored channel structures based on gyroids for non-premixed ammonia combustion.

2. Materials and methods

2.1. Sample preparation

The ceramic raw materials used for the sample manufacturing were tabular alumina T60/64 (Almatis, Germany, 0–20 µm, d_{50} = 4.33 µm, d_{90} = 13.61 µm, specific surface: 3.32 m^2 g^{-1}), reactive alumina CT 3000 LS SG (Almatis, Germany, d_{50} = 0.49 µm, d_{90} = 6.55 µm, specific surface: 7,98 m^2 g^{-1}), a magnesia-stabilized zirconia (Saint-Gobain, France, d_{50} = 0.19 µm, d_{90} = 4.53 µm, 38 wt % tetragonal phase, 62 wt % cubic phase) and a titania (TR, Crenox GmbH, Germany, d_{50} = 1.27 µm, d_{90} = 3.94 µm). The thermoplastic binder system was predominantly composed of two types of low density polyethylene (LDPE, Rowak AG, Germany) with the specifications H70 (melting range: 100 – 104 °C) and H150 (melting range: 98 – 102 °C). Additionally, the following additives were admixed to improve the manufacturing process and the dimensional stability of the samples during the subsequent thermal treatments: Cellulose (Sigma-Aldrich, Germany) used as backbone material, stearic acid ($\geq$ 98 %, Carl Roth, Germany) as lubricant and ammonium ligninsulfonate (ALS C12C, Otto Dille, Germany) as temporary binder. The compositions of the sample batches designated as A1 (tabular alumina), A2 (reactive alumina) and A3 (AZT) are presented in Table 1. Composition A2 (reactive alumina) required a higher binder content of 50 vol % to produce a thermoplastic mass due to the higher specific surface of the used alumina raw material compared to the compositions A1 and A3. The fractions of ZrO_2 and TiO_2 in composition A3 (AZT) given in vol % in Table 1 (corresponding to the common feedstock nomenclature) are equal to 2.5 wt % each related to the total fraction of ceramic raw materials according to former studies [12].

The pellet fabrication was realized in several steps according to previous studies [24]. At first, the raw materials were premixed at room temperature by means of an Eirich laboratory mixer EL-1 (Maschinenfabrik Gustav Eirich, Germany) with a rotation speed of 500 rpm and a mixing time of 5 min. Afterwards, the premixed raw materials were transferred into a thermoplastic mass by a single screw extruder type LK III 2A (Linden, Germany) equipped with an additional mixing chamber and two Z kneader blades. For this purpose, the mixing chamber was heated up to 133 (± 3) °C and the raw materials were mixed and homogenized at 20 rpm for 30 min. The thermoplastic mass was then extruded with a speed of 5 rpm through a die with 8 horizontal-aligned channels each having a diameter of 2.5 mm. The die was additionally heated up to a temperature of 103 °C to avoid solidification effects during the extrusion. The extruded strands were manually cut into pellets with a maximum length of up to 5 mm, which were used for the sample manufacturing without further post-processing.

In order to evaluate and compare the material properties in dependence on the chemical composition and in advance of the production of complex structures, simple bulk samples were manufactured and investigated. The samples geometries were designed by means of SolidWorks 2018 (2017 (Dessault Systemes SolidWork Corp., France) and sliced with the aid of the software Ultimaker Cura (version 5.6.0., Ultimaker, Netherlands). As presented in Fig. 1, two plate geometries with the dimensions 70 × 7.35 × 2.4 mm^3 and 20 × 7.35 × 2.4 mm^3 were generated. Both sample geometries were modelled with a notch (length of 10 mm and width of 1.05 mm) placed centrally and orthogonally to the front side (7.35 × 2.4 mm^2) to ensure a proper sample positioning in future tests in ammonia combustion atmosphere.

Table 1
Sample compositions.

Raw Material	Type	A1 in vol %	A2 in vol %	A3 in vol %
Al_2O_3	T60/64	52.00		49.91
	CT3000SG		50.00	
ZrO_2				0.89
TiO_2				1.20
Polyethylene	LDPE 70	20.70	20.94	20.70
	LDPE 150	12.42	12.56	12.42
Cellulose		9.60	10.00	9.60
Steric acid		4.80	6.00	4.80
Ligninsulfonate		0.48	0.50	0.48
Total binder content		48	50	48

The manufacturing of the plate samples was conducted by means of a Fused Granulate Fabrication (FGF) printer of the type M.A.T. (3D Ceram, France), which was equipped with one printing head and possessed a maximum building volume of 200 × 200 × 200 mm^3. The printing nozzle exhibited a diameter of 1.0 mm. The printing was carried out concentrically from outside to inside with an infill density of 100 % without heating the building chamber. The printing parameters in dependence on the individual composition are listed in Table 2.

The removal of the organic binder materials was conducted exclusively thermally in a two-step debinding procedure under air. In order to avoid the formation of cavities within the sample structure due to boiling and degassing effects as shown in previous studies [24,28] the samples were embedded in an alumina bed (T60/64, Almatis, Germany, $d < 20$ µm) and partially debinded up to a temperature of 220 °C with a heating rate of 5 K min^{-1} under air atmosphere. Afterwards, the samples were removed from the alumina bed and completely debinded at temperatures up to 480 °C by means of an air-ventilated furnace (Xerion, Germany). The air flow was kept constant at 10 dm^3 min^{-1}. Subsequently, the samples were sintered at 1600 °C in air atmosphere. Table 3 presents a detailed overview of the debinding and sintering regimes. The samples were positioned on a corundum particle bed during the second debinding step and the sintering process.

2.2. Sample characterization

The bulk density was determined by means of the Archimedes principle in accordance to DIN EN 993–1 using water as fluid (21 °C).

The evaluation of the mechanical properties was realized by determining the flexural strength and the Young's modulus at room temperature. For this purpose, 5 samples of each composition batch (70 × 7.35 × 2.4 mm^3) were tested in the sintered state as well as after one and five thermal shocks. The three-point flexural strength was determined using the universal testing machine TT28100 (TIRA GmbH, Germany) equipped with a 1 kN load cell. According to DIN EN 993–5, the distance between the bearings was 40 mm and the samples were placed excluding the notched part or parts deviating from the cuboid shape. The tests were conducted at a displacement-controlled rate of 1 mm min^{-1} until a force drop of 80 % relative to the maximum load was registered. The dynamic Young's modulus was examined by means of the impulse excitation technique (flexure mode) according to DIN EN 843–2. The measurements were conducted 10 times for each sample.

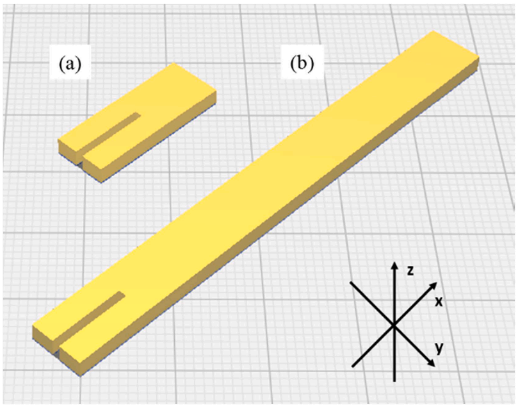

Fig. 1. Schematic draft of the model samples (size 70 × 7.35 × 2.4 mm^3).

Table 2
Printing parameters.

Parameter		A1	A2	A3
Printing temperature in °C	Layer 1	190	180	190
	Layer 2+	175	175	175
Printing bed temperature in °C		70	70	70
Material flow in %	Layer 1	110	100	110
	Layer 2+	100	94	100
Printing speed in mm/s		20	20	20

Table 3
Debinding and sintering regimes.

Tempature in °C		Heating rate	Dwell time at end temperature
Start	End	in K min^{-1}	in min
First debinding step			
20	90	1.0	30
90	220	5.0	60
220	20	free	
Second debinding step			
20	220	3.0	
220	480	0.2	90
480	20	3.0	
Sintering			
20	460	3.0	
460	600	0.5	
600	900	3.0	
900	1600	1.0	240
1600	20	1.0	

The pore size distribution was determined by means of mercury intrusion porosimetry (Autopore V 9620, Micromeritics Instrument Corp., Norcross, Georgia, USA). Sample fragments after flexural strength tests were used for the measurements to allow an initial filling of macrocavites to realize the determination of the pore size distribution of the bulk material.

The thermal shock behavior of the samples was tested according to DIN EN 993–11. The samples were placed in a furnace at 1100 °C. After 45 min, the samples were removed and immediately positioned below a nozzle releasing compressed air (2 bar) for 5 min. The distance between the samples and the nozzle was approx. 200 mm. Although the service conditions during ammonia combustion include higher maximum temperatures up to 1500 °C, the thermal shock tests from 1100 °C to room temperature provide information for the comparison of the different materials while considering occupational safety and are an established procedure in the area of high temperature ceramics. Additionally, quenching of the samples with compressed air ensures a more consistent temperature of the quenching medium (air) and thus a higher temperature gradient due its high flow velocity during the tests, whereas the temperature gradient during cooling in case of ammonia combustion at similar temperatures is estimated lower due to the heating of the surrounding air. Since the compressed air could provoke an uncontrolled movement and blowing away of the samples, they were placed between two rectangular steel frames with a mesh (mesh size of 1.5 mm) during the entire experiment. This procedure was conducted once (designated as “1 TS”) or five times (designated as “5 TS”) for 5 samples of each batch. The Young’s modulus, the flexural strength and the pore size distribution were examined after sintering as well as after one and five thermal shock tests.

The visualisation and evaluation of the determined data for the elastic modulus and the flexural strength were done with the help of box plots [29]. The box represents the interquartile range (IQR) where the lower and upper edges represent the first and the third quartile of the data set, respectively. The line within the box corresponds to the second quartile equalling the 50th percentile or median. The whiskers are lines from the box edges to the most distant data point of the data set which is still within 1.5 interquartile ranges from the box edges. Data points further beyond 1.5 interquartile ranges are called outliers and marked by dots. To evaluate differences in the evolution of the mechanical properties of the sample series, a non-overlapping of boxes was considered as relevant difference in the sample properties.

The analysis of the microstructure was performed by means of a digital light microscope of the type VHX-2000 D (Keyence, Belgium) equipped with a VH-Z20R objective. Furthermore, scanning electron microscope (SEM) investigations were conducted using the device ESEM FEG XL30 (Phillips, Netherlands). For this, the cross-sections of sample fragments of each composition batch obtained from the three-point flexural strength tests were investigated. Furthermore, sample fragments were embedded in epoxy resin, grinded and polished. They were analyzed with regard to phase composition using electron backscatter diffraction (EBSD, Bruker Nano GmbH, Germany) and energy-dispersive x-ray spectroscopy (EDX, Bruker Nano GmbH, Germany) on an SEM Amber (Tescan, Czech Republic).

2.3. *Ammonia combustion test*

In order to characterize the chemical alteration of the alumina-based compositions during ammonia combustion, sintered samples (20 × 7.35 × 2.4 mm^3) of each batch were tested in a heated slot burner, which is described in detail by Kretzler et al. [20]. The slot burner has a combustion zone with the dimensions of 150 × 10 × 250 mm^3. A splitter plate separates the ammonia and air inflows for non-premixed operation. The samples were fixed by a ceramic rod (Al_2O_3, diameter 1 mm) through a small hole in the samples. The samples were exposed for 1 h to an NH_3/air flame characterized in Kretzler et al. [20], operated at a thermal load of 0.6 kW and the maximum oven set temperature, corresponding to gas-phase temperatures >1500 °C at the sample location. After exposure, the samples were freely cooled down to room temperature. The tested samples were investigated regarding their microstructure, chemical composition and phase composition by SEM analyses using EDX and EBSD (see Section 2.2).

2.4. *Manufacturing of model components*

Model components based on sheet-gyroid structures with a gas supplier system were generated using the software MSLattice [30] with a size of 3 × 3 × 3 cells, a relative density of 25.29 % and a mesh density of 90 points. A side wall construction and gas connectors were added using the software FreeCAD (version 0.21.2, Jürgen Riegel). The obtained stl.-files were translated into .gcode-files using the open source software UltimakerCura (version 5.6.0., Ultimaker, Netherlands). The construction was scaled to 29.8 × 29.8 × 28.3 mm^3 (without supplier tubes) as shown in Fig. 2. Based on the results of the thermomechanical properties of the bulk samples, the most promising composition A1 was selected for the model component fabrication. The manufacturing was conducted using the composition A1 (tabular alumina) on a M.A.T. (Multi Additive Technology) printer (3D Ceram, France) equipped with a single extruder (printing nozzle diameter of 0.6 mm) and a building volume of 200 × 200 × 200 mm^3. The printing parameters for A1 (tabular alumina) from Table 2 were applied. Debinding and sintering was done according to the procedure described in Section 2.1 and shown in Table 3.

The samples were analyzed in the sintered state without further post-treatment using a microfocus X-ray computer tomograph CT-ALPHA (Procon X-Ray, Germany). The tomographic scans were performed with a 160 kV X-ray source and a flat detector Dexela Type 1512 (PerkinElmer, Germany) with 1944 × 1526 active pixels. The reconstructed CT image has a voxel size of 23.17 μm × of 23.17 μm x of 23.17 μm.

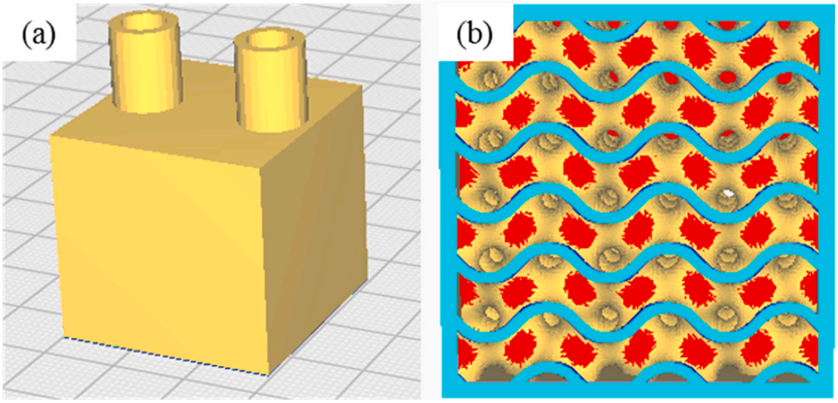

Fig. 2. Model component for burner applications – digital model, cube side length: 30 mm.

3. Results and discussion

3.1. Sample properties after manufacturing

The sample manufacturing by means of FGF enabled the printing of the intended geometry independently of the chemical compositions of the feedstock. Only for the composition A2 (reactive alumina), the flow had to be reduced for both the first layer and the following layers compared to the other compositions based on tabular alumina. Although the reactive alumina exhibited a smaller grain size and thus a higher specific surface, the higher binder volume fraction (see Table 1) resulted in a decrease of the temperature required to achieve a similar thermoplastic behavior as the compositions with tabular alumina and thus, the material flow had to be adjusted accordingly (Table 2). Nonetheless, the created sample geometries were similar to those of the digital model for all compositions. There were only some deviations near the notch. In order to ensure a sufficient adhesion of the material to the printing bed, the samples were manufactured with the aid of a brim and a higher flow rate for the first layer (see Table 2). Both parameter configurations resulted in a closing of the notch within the first layer and thus entailed a post-processing step to re-open it using a razor blade.

The debinding and sintering steps were accomplished according to Table 3 for all sample geometries and yielded the intended prismatic samples for the three investigated material systems (see Fig. 3). Hence,

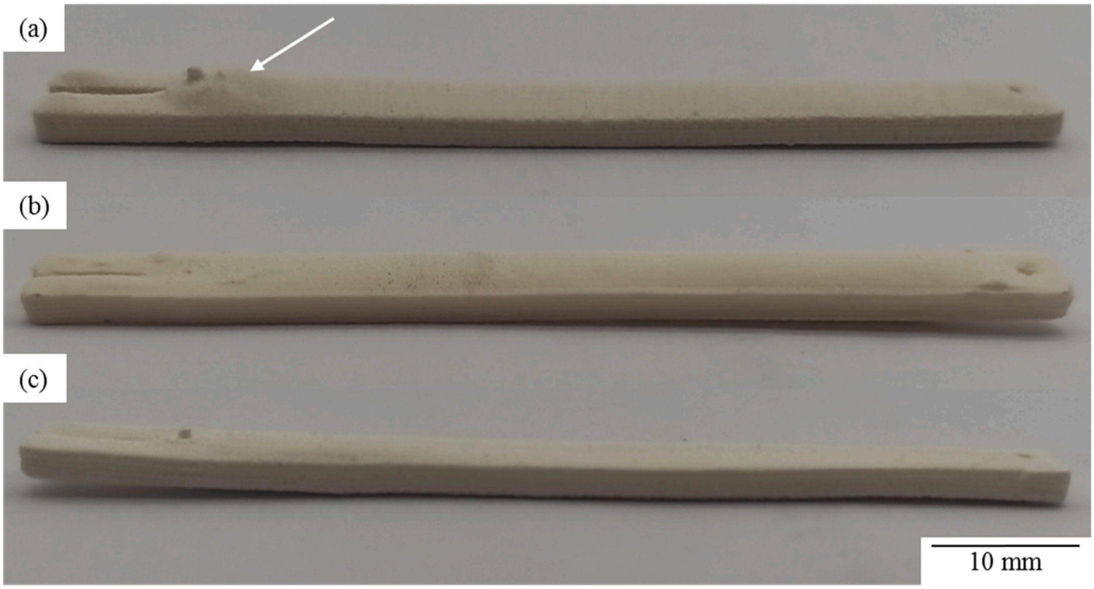

Fig. 3. Images of prismatic, notched samples (20 × 7.35 × 2.4 mm^3) composed of (a) A1, (b) A2 and (c) A3; cavity formation due to layer transition during the printing process marked by arrow.

Table 4
Physical sample properties after sintering.

		A1	A2	A3
Shrinkage in %	x-direction	11.86 ± 0.01	15.01 ± 0.01	14.07 ± 0.01
	y-direction	14.82 ± 0.02	18.46 ± 0.01	15.46 ± 0.02
	z-direction	−5.03 ± 0.23	−22.02 ± 0.22	−9.14 ± 6.51
Bulk density in g cm^{-3}		2.44 ± 0.07	2.73 ± 0.16	2.55 ± 0.27
Young's modulus in GPa		105.68 ± 9.16	210.35 ± 12.94	31.29 ± 5.15
Flexural strength in MPa		49.35 ± 6.51	102.14 ± 25.67	7.99 ± 2.05

the binder system and the thermal debinding regime from previous studies covering material systems based on tabular alumina [24,26,27] similar to A1 of this study can be applied as shaping technology for the fine-grained alumina system (A2) and the AZT system (A3).

Table 4 presents the physical properties of the manufactured samples. The shrinkage in x-direction is in the range of 11.5 - 15 % and in y-direction in the range of 14.5 - 18.5 %. This is in the same order of magnitude as in the previous study [24] and confirms the previous data. However, there are differences between the three compositions. In both planar directions, the shrinkage is highest for composition A2 (reactive alumina), whereas it is lowest for composition A1 (tabular alumina). The deviations in the shrinkage in x- and y-direction for all samples are attributed to the internal linear structure of the samples due to the line based printing process as well as friction phenomena between the samples and the corundum particle bed used as sintering aid. The shrinkage in z-direction (height) has for all sample types a negative value corresponding to a volume expansion. These data will be discussed later on in relation to the mechanical properties.

Fig. 4 presents SEM images of the microstructures of compositions A1 (tabular alumina, Fig. 2a), A2 (reactive alumina, Fig. 2b) and A3 (AZT, Fig. 2c), which help understanding the observed differences in shrinkage in x- and y-direction. It can be seen that A2 (reactive alumina) and A3 (AZT) exhibited a microstructure of a higher sintering degree with a low interparticle microporosity whereas the Al_2O_3 grains were less sintered in case of A1 (tabular alumina) accompanied with a higher interparticle microporosity. Regarding A2 (reactive alumina), the smaller grain size of the Al_2O_3 raw material ($d_{50} = 0.49$ μm, $d_{90} = 6.55$ μm) induced an increased sinter activity leading to a higher sintering degree of the microstructure and thus, a higher densification and the highest shrinkage values in the planar directions. The differences of the A1 (tabular alumina) and A3 (AZT) microstructures, both using the same tabular alumina as Al_2O_3-source, were attributed to the presence of TiO_2 located between Al_2O_3 grains. According to the literature [31–33], TiO_2 diffuses in the Al_2O_3 grains at temperatures above 1500 °C and acts as sintering agent resulting in Al_2O_3 grain growth. For this reason, a larger Al_2O_3 grain size was found within the A3 (AZT) microstructure (up to 40 μm) compared A1 (tabular alumina) (up to 20 μm). This contributed also to a lower interparticle microporosity of A3 (AZT) samples compared to A1 (tabular alumina) although the same Al_2O_3 raw material was used.

The measured bulk densities confirmed this observation. The highest bulk density was reached for A2 (reactive alumina) due to its low initial grain size distribution causing an increased sintering activity. In contrast to this, A1 (tabular alumina) showed a smaller bulk density. However, A3 (AZT) underwent a higher densification compared to A1 (tabular alumina) although the same raw alumina was used resulting from the intensification of the sintering processes due to the TiO_2 doping. This effect of grain coarsening and densification of A3 (AZT) could be enhanced (up to 100 μm) by using raw materials with a finer particle size distribution having a higher reactivity as shown in former studies [12].

Furthermore, Table 4 presents the flexural strength and the Young's modulus of the samples, which differed for the three materials. A2 (reactive alumina) exhibited the highest mechanical values. This corresponded well to the measured bulk density and shrinkage showing the highest densification for A2 (reactive alumina). However, for A1 (tabular alumina) and A3 (AZT) this relation did not exist, since A3 (AZT) yielded the better densification but had a lower mechanical performance. Therefore, cross-sections were analyzed for each sample type by digital light microscopy as exemplarily presented by Fig. 5 and pore size distributions were registered by mercury intrusion porosimetry, shown in Fig. 6 and Table 5, to gain a deeper understanding of the relation between mechanical properties and pore structure of the three materials.

Two dominant pore types were identified within the sample structures by digital light microscopy. Firstly, triconcave pores were found between the individual strands of two consecutive layers for all sample compositions due to the elliptical cross-section of the strands. They are especially visible for example in Figs. 5a and 5b. Their edge length was in the order of magnitude of 100–300 μm. These triconcave pores were of particular importance for the debinding procedure since they crossed the entire sample volume and thus formed a pore channel structure. These channel structures enabled the transport and release of the gaseous products from the interior sample volume formed during the thermal decomposition of the organic binder materials [24].

Secondly, large cavities were observed especially within the A2 (reactive alumina) samples, which separated two consecutive layers. Their dimensions were in the range of 150–1000 μm where the maximum extension was typically in the planar directions x and y. In case of A1 and A3, similar but smaller cavities were found at the last

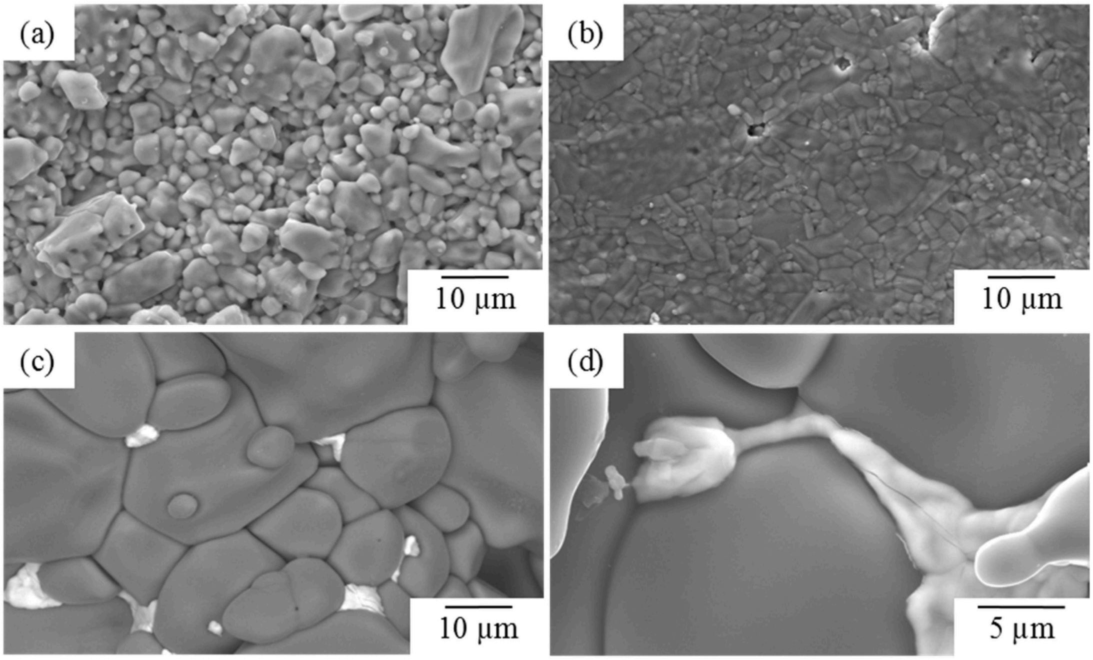

Fig. 4. SEM images (mixed mode) of the (a) A1 (tabular alumina), (b) A2 (reactive alumina) and (c,d) A3 (AZT) sample cross-section after sintering.

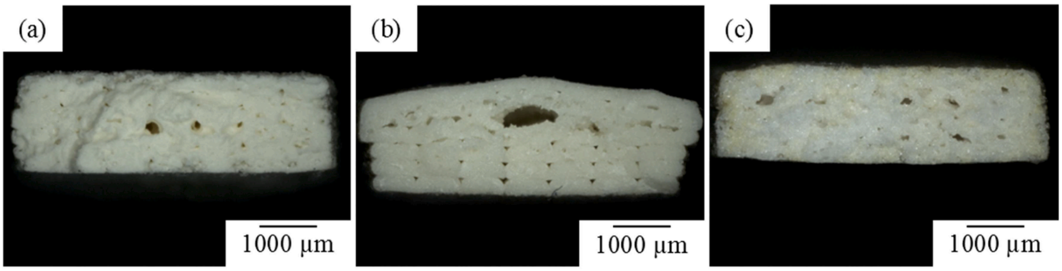

Fig. 5. Images of the (a) A1, (b) A2 and (c) A3 sample cross-sections after sintering and flexural strength measurements (broken cross-section surface) recorded by digital light microscopy.

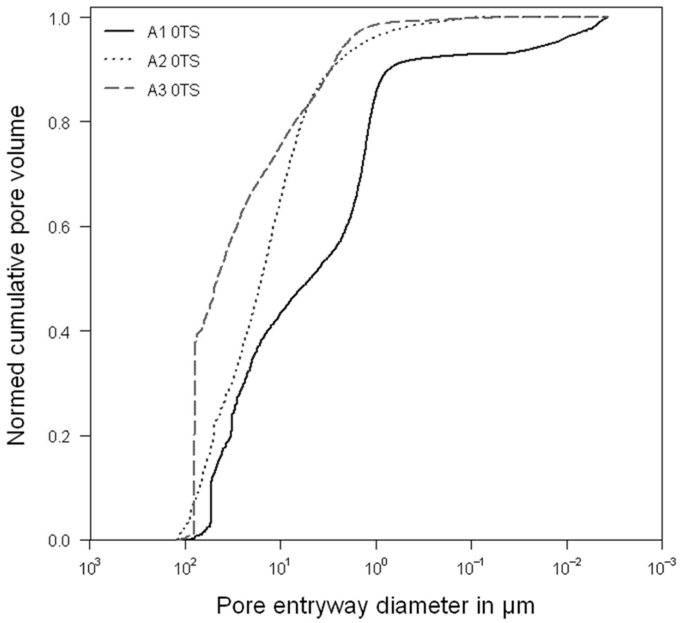

Fig. 6. Normed cumulative pore entryway distribution of A1, A2 and A3 after sintering measured by MIP.

Table 5
90th and 50th percentile of the cumulative pore entryway distribution after sintering (0 TS) as well as 1 TS and 5 TS (d_x corresponding to x % of the open pores with a pore entryway larger than d_x).

	Sintered state (0 TS)			After 1 TS			After 5 TS		
	A1	A2	A3	A1	A2	A3	A1	A2	A3
d_{50} in μm	4.9	15.8	45.8	4.0	11.3	24.1	6.1	12.5	28.3
d_{90} in μm	0.7	3.0	3.0	0.9	2.1	2.4	0.9	0.1	2.5

printing point of a layer at which the sample manufacturing was paused to move the printing bed downwards for the deposition of the subsequent layer (marked by arrows in Fig. 3). Since the cavity formation was initiated within the temperature range of 120 – 140 °C during the first debinding [23], it was considered that LDPE melted and partially closed the triconcave pores originating from the positioning of the thermoplastic strands during the printing process. Thus, the release of volatiles formed during the thermal decomposition of the organic binder materials was blocked. Furthermore, the ceramic particles in the A2 samples (reactive alumina) were finer than for A1 (tabular alumina), resulting in a denser microstructure of the printed sample hindering the gas permeation during the debinding step [34]. These effects resulted in a pressure increase within the structure. Since the bonding between the single layers is based on the adhesion caused by the molten binder components during the printing process, the pressure increase exceeded the interlayer bonding strength. Because of the maximum extension of the large cavities in x- and y-direction it was considered that the connection between strands within one layer in the x-y-plane was more effective than between layers what corresponded to comparably higher adhesive forces within a layer. This was related to the printing process as the relatively low temperature difference between subsequently printed neighboring strands enhances the formation of a good connection between the strands and promotes the interstrand adhesion in the x-y-plane. The printing of the subsequent layer starts at a random position on the perimeter of the previous layer. At this position, cooling processes had already started resulting in a higher temperature difference between the newly deposited strand and the surface of the previous layer compared to neighboring strands within one layer, which resulted in reduced adhesive forces between the layers. Consequently, the layers were preferentially separated from each other causing the formation of cavities during thermal debinding and led to an expansion of the samples in height (z-direction) being still persistent after sintering as shown in Table 4.

Based on the higher binder content of A2 (reactive alumina) compared to the other compositions (Table 1), a more pronounced closure of the triconcave pores and the generation of a higher volatile amount occurred within the A2 (reactive alumina) structure resulting in a more excessive height expansion (negative shrinkage in z-direction in Table 4) and the formation of macropores in the material.

Fig. 6 presents the results of the mercury intrusion porosimetry measurements. The investigations revealed a maximum pore size of approximately 100 μm. Since the triconcave pores and large cavities exceeded this size, the registered pores were predominantly identified as porosity of the bulk material of the strands. The pore size distributions differed between the three compositions. A1 (tabular alumina) has a finer pore size distribution with a higher fraction of small pores than the other two compositions, which is shown by the lowest values for d_{90} and d_{50} in Table 5 compared to the other two compositions. This corresponds well to the comparably lower sintering activity and the resulting fine intergranular pores visible in Fig. 4a for A1 (tabular alumina). Furthermore, it exhibits a slightly bimodal character. A2 (reactive alumina) and A3 (AZT) have a much lower fraction of fine pores in the stand material due to their higher sintering activity related to the finer initial grain size in the case of A2 (reactive alumina) and the effect of TiO_2 as sintering aid for A3 (AZT). This is reflected by the low interparticle porosity in Figs. 4b and 4c.

For A2 (reactive alumina), the high sintering activity causes two remarkable issues in relation to the high expansion in height of the sintered samples in comparison to the other two compositions. Firstly, the high expansion in z-direction was overcompensated by the planar shrinkage in x- and y-direction, which was highest for A2 compared to the other two samples. This resulted in the highest bulk density of the three material types and a low fraction of fine pores in the sintered state in spite of the high expansion in height (Table 4). Secondly, the high expansion in z-direction related to the formation of macroscopic cavities in the A2 (reactive alumina) samples did not dominate the mechanical performance. The densification of the solid material during the sintering step was so efficient, that the material had a better performance than A1 (tabular alumina) (see Table 4), although A1 (tabular alumina) showed much less expansion in height corresponding to less macropore formation in the samples.

Regarding A3 (AZT), the investigated cross-sections showed pores in the same order of magnitude as the triconcave pores of A1 (reactive alumina) and no irregular macropores, which corresponded well to the relative low expansion in z-direction (Table 4). It was assumed that the high shape diversity of the formed pores is related to the finer grain size of the TiO_2 and ZrO_2 fraction of the AZT system compared to the tabular alumina used as Al_2O_3-source. The presence of fine TiO_2 and ZrO_2 particles led to a densification of the microstructure in the corresponding regions in the printed state. Thus, the gas permeation rate was reduced in some areas of the sample and the gas transport of the binder decomposition products out of the sample structure was hindered [34]. This effect lead to a local pressure increase within the structure causing the formation of cavities during thermal debinding and explained also the higher expansion in z-direction of the A3 (AZT) samples compared to A1 (tabular alumina).

For understanding the low values of flexural strength and Young's modulus of A3 (AZT) compared to the other two sample compositions, the differing phase composition compared to the pure alumina systems has additionally to be taken into account. For a more detailed characterization, the microstructure was investigated by means of EBSD. As expected from the raw materials, A1 (tabular alumina) and A2 (reactive alumina) were completely composed of corundum, whereas A3 (AZT) contained multiple phases as shown in Fig. 7.

The main phase of the structure was corundum (pink) containing traces of TiO_2, which underlines the diffusion of TiO_2 within the Al_2O_3 grain during sintering and its role as sintering aid, which resulted in the low fraction of fine pores in the pore size distribution (Table 5). At the interface between the Al_2O_3 and TiO_2 (green) grains, the formation of Al_2TiO_5 (yellow) was observed, which forms a stable phase due to a solid-state reaction of Al_2O_3 and TiO_2 at temperatures above 1280 °C [11]. ZrO_2 (blue) was not involved in this reaction but changed from its initially cubic and tetragonal state into the monoclinic state. According to Aneziris et al. [9], TiO_2 is incorporated into the ZrO_2 lattice at temperatures above 1500 °C and leads to the removal of MgO used as stabilizing agent. Consequently, a destabilization of ZrO_2 is promoted

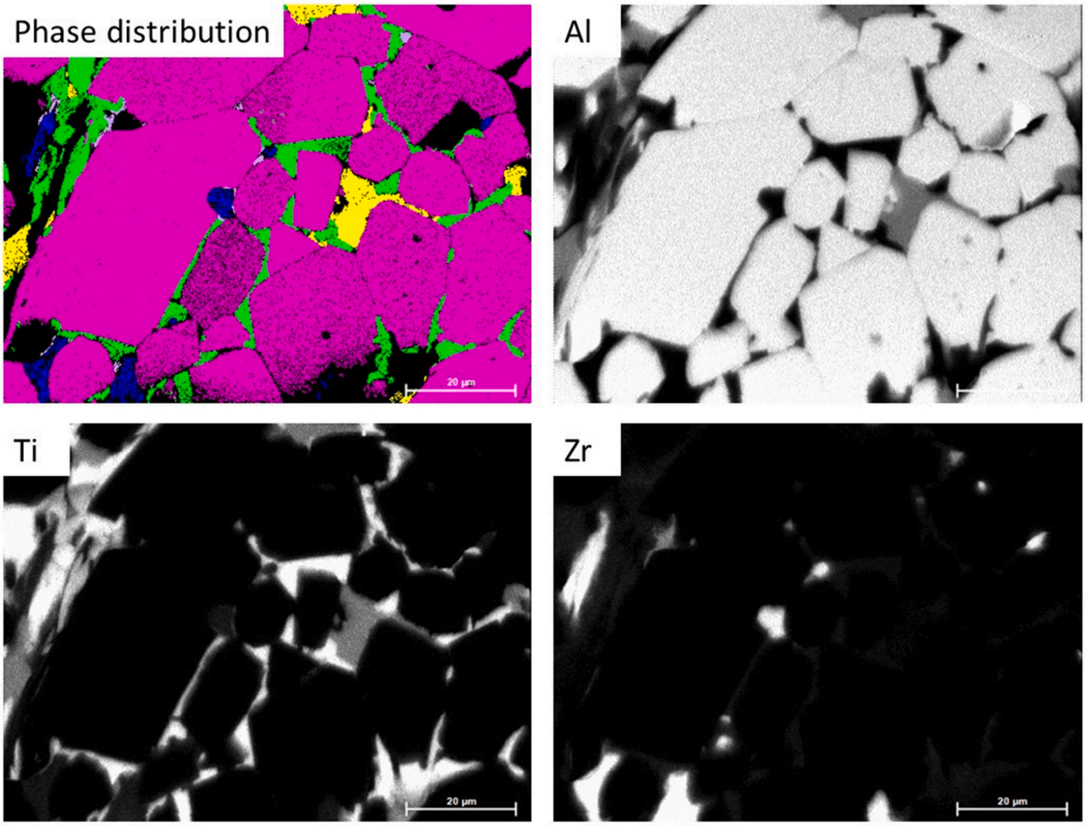

Fig. 7. EBSD and EDX analysis for A3 (AZT) in the sintered state, phase distribution: pink – corundum, blue – monoclinic ZrO_2, green – TiO_2, yellow – Al_2TiO_5, purple – $ZrTiO_4$.

resulting in the phase transformation. This assumption was supported by the identification of $ZrTiO_4$ (purple), which occurred as small grains ($<$ 2 μm) at scattered spots.

According to previous studies [9] and further data from the literature [35], the formation of Al_2TiO_5 leads to the introduction of thermal stresses due to its anisotropic thermal expansion coefficients along the crystallography axes. Moreover, the phase transformation of ZrO_2 is also accompanied with a shift of the thermal expansion coefficients, whereby thermal stresses arise. Additionally, the formation of the low temperature monoclinic phase goes along with a volume change of approximately 3–5 vol % resulting in mechanical stresses. These thermal and mechanical stresses provoked the emergence of microcracks within the A3 (AZT) structure as presented in Fig. 4d. The microcracks contributed to a weak microstructure with uniformly distributed inhomogeneities resulting in a comparably low level of the mechanical sample properties.

The presence of these microcracks is also apparent in the pore size distribution. A3 (AZT) had the highest value for d_{50} correlating with a higher fraction of coarser cavities compared to the other compositions. They correspond to the formed microcrack network. Furthermore, the initial filling of the open pores in the sample with mercury showed an almost vertical section of the normed cumulative pore volume curve in Fig. 6. This is probably related to the applied pressure causing a local exceeding of the mechanical strength, a breaking of the microcracked material and a filling of suddenly created cavities in the material resulting in the steep increase of the curve. Thus, the A3 (AZT) samples should exhibit lower d_{50} and d_{90} values compared to the measured data by MIP and the accuracy is limited. Therefore, the specific percentile values were considered as an estimate, but the resulting order of magnitude and observed trends were regarded as a reliable result.

The physical properties of the investigated sample compositions after sintering can be summarized as follows: The thermal decomposition of the binder materials caused a volume expansion in height (z-direction) due to the formation of gaseous products, which was more pronounced with a finer particle size distribution of the ceramic material system. In the horizontal dimensions (x- and y-direction), A2 (reactive alumina) as finest raw material system was subjected to the highest shrinkage followed by A3 (AZT) due to its varying particle sizes and sinter reactivity of its multi-component raw material mixture. Based on the specific microstructure formation during sintering, the A2 (reactive alumina) and A3 (AZT) samples exhibited a higher bulk density compared to A1 (tabular alumina). Regarding the mechanical sample properties, distinct differences in the Young's modulus and flexural strength were determined. While the highest values were found for A2 (reactive alumina) due to a higher sintering degree and lower interparticle porosity, A3 (AZT) evinced considerably lower values for the Young's modulus and the flexural strength compared to A1 (tabular alumina) and A2 (reactive alumina). These results were predominantly attributed to the presence of secondary and newly formed phases exhibiting differences in the thermal expansion coefficients and hence causing the formation of microcracks in the AZT (A3) microstructure.

3.2. Sample properties after thermal shocks

In order to evaluate the thermal shock performance under application-near conditions, the three materials were quenched up to five times from 1100 °C to room temperature by means of compressed air. All tested samples survived five thermal shocks without failures or macroscopic defects.

For the evaluation of the thermal shock resistance, the Young's modulus and the flexural strength were determined in dependence on the number of thermal shocks. Figs. 8a and 9a presents the data for the three materials after sintering (0 TS), one (1 TS) and five (5 TS) thermal shocks. Table 6 shows the losses in the Young's modulus and flexural strength after 1 TS and 5 TS related to the sintered state as well as the losses after 5 TS related to the state after 1 TS. Additonally, box plots were used (Figs. 8b and 9b) to evaluate the evolution of flexural strength and Young's modulus for each sample compostion with increasing number of thermal shock tests. A non-overlapping of boxes was considered as relevant difference in the sample properties due to the applied thermal shock cycles.

The elastic modulus with its evolution during thermal shock cycles is an important design-relevant mechanical parameter to describe the thermal shock behaviour of materials and their elastic capabilities. Thermal shock load causes thermal stresses in the components, which result from temperature gradients created during the shocking process [36]. The formed thermal stresses σ_{th} depend on the applied temperature difference ΔT and on material properties. These are the thermal expansion behaviour expressed by the thermal expansion coefficient α and the elastic behaviour described by the elastic modulus E. The relation is expressed by Eq. (1). In general, a high dimensional stability and a high fracture strain typically resulting from a low elastic modulus are desired properties for materials during temperature changes under service. Overall, the application of thermal stresses on ceramic materials damages the microstrucutre by crack initiation or crack growth due to the sensitivity of ceramic materials to tensile stresses, which are especially relevant for the rapid cooling of downward thermal shocks [36, 37]. On the long term, these processes have a detrimental effect on the microstructure, the mechanical performance and the integrity of the ceramic component.

$$\sigma_{th} = \alpha \cdot E \cdot \Delta T \tag{1}$$

The expected changes in the microstructure due to thermal load are caused by thermal stresses and additional phase transformations in the case of A3 (AZT) – see Section 1. Both result in the growth of already present cracks or the initiation of new cracks. The expected phase transformations at elevated temperatures are related to volume changes,

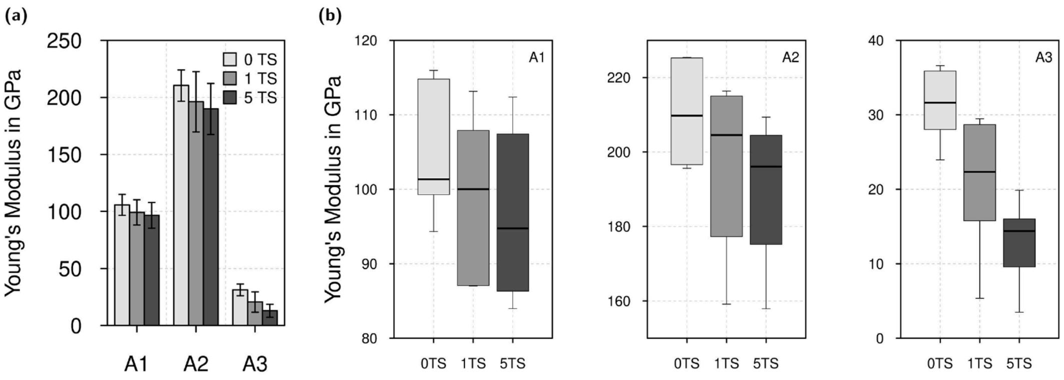

Fig. 8. (a) Young's modulus and (b) box plot representation of the Young's modulus of A1, A2 and A3 samples after sintering (0 TS), one thermal shock (1 TS) and five thermal shocks (5 TS).

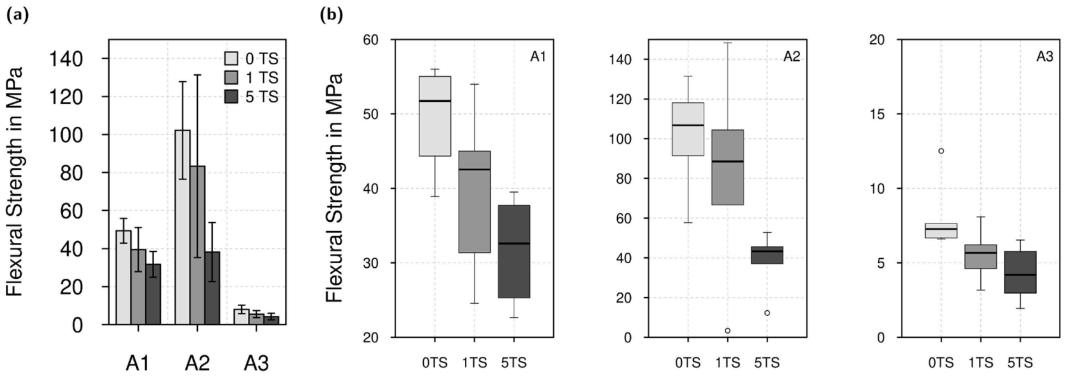

Fig. 9. (a) Flexural strength and (b) box plot representation of the flexural strength of A1, A2 and A3 samples after sintering (0 TS), one thermal shock (1 TS) and five thermal shocks (5 TS).

Table 6
Changes of Flexural strength and Young's modulus of A1, A2 and A3 samples after one thermal shock (1 TS) and five thermal shocks (5 TS) related to the sintered state (0 TS → 1 TS and 0 TS → 5 TS) and after 5 TS related to 1 TS (1 TS → 5 TS), underlined values correspond to relevant changes.

Parameter	Thermal shock step	A1	A2 Loss in %	A3
Young's modulus	0 TS → 1 TS	6.1	6.8	34.0
	1 TS → 5 TS	2.6	3.2	37.3
	0 TS → 5 TS	8.6	9.8	$\underline{58.6}$
Flexural strength	0 TS → 1 TS	20.0	18.5	$\underline{30.5}$
	1 TS → 5 TS	19.7	$\underline{54.1}$	23.2
	0 TS → 5 TS	$\underline{35.7}$	$\underline{62.6}$	$\underline{46.6}$

e.g. the decomposition of Al_2TiO_5 is accompanied by a volume shrinkage, the modification change of ZrO_2 from the tetragonal to the monoclinic phase causes a volume expansion of 3–5 vol %. These dimensional changes cause stresses in the surrounding material, which is expected to enhance the microcrack formation. These cracks correspond to fine cavities in the material, which have the same effect as pores on the elastic modulus at room temperature. With increasing porosity, the elastic modulus decreases. The measurement of the elastic modulus was used as non-destructive method at room temperature to evaluate such changes in the microstructure, which formed during the influence of thermal load.

Regarding Young's modulus of the investigated samples, Fig. 8a shows that the three material systems differ strongly in their elastic modulus level. A2 (reactive alumina) exhibted the highest total values due to the high sintering degree and the low interparticle microporosity, whereas the lowest values were observed for A3 (AZT) based on the aforementioned phase alterations and resulting microcrack formation during sintering.

Fig. 8b presents the box plots of the Young's modulus depending on the applied number of thermal shocks. For A1 (tabular alumina) and A2 (reactive alumina) the boxes overlap strongly, which is considered as a non-relevant change in the elastic modulus. The slight decreasing trend of the values for both material systems corresponds to the beginning changes of the microstructure due to the applied thermal stresses. Overall, the data show that the elastic modulus stays close to the initial value for up to 5 thermal shocks. The remaining of the elastic modulus close to its initial level is a desired property for refractory materials. According to Larson et al. [38] the elastic modulus is an essential material specific factor, which determines the thermal shock behaviour of a refractory material. It is a relevant factor for the material's potential to arrest cracks (small initial crack size) or to retain the initial critical temperature difference at which larger cracks would start propagating [38]. The remaining of the elastic modulus as long as possible close to its initial level preserves this potential, which is important for surviving multiple thermal shocks.

Concerning A3 (AZT) the decreasing trend in Young's modulus is more pronounced, which is also shown by the higher loss due to the applied thermal shocks compared to the other two compositions (see Table 6). However, the comparison of the box plots yields that a relevant decrease in elastic modulus occurred only by comparing the samples after sintering (0 TS) and 5 TS, as the corresponding boxes do not overlap. In contrast, the comparison of the states after 0 TS and 1 TS as well as after 1 TS and 5 TS show still an overlapping. These data yield that the loss in elastic modulus takes place gradually and decreases per additional thermal shock. The results are in agreement with the data shown in Table 6, which presents a similar loss of 34.0 % and 37.3 % after one (0 TS → 1 TS) and after four thermal shocks (1 TS → 5 TS), respectively. This means that further occuring thermal stresses were relieved more efficiently by the subsequent microstructural state formed after 1 TS. Thus, a further relevant degradation in terms of elastic modulus for up to five thermal shocks cannot be shown, which corresponds to the overlapping of the boxes after 1 TS and 5 TS (Fig. 8b). This persisting of the elastic modulus after the first damaging effects is relevant for the potential of A3 (AZT) to arrest cracks (small initial crack size) or for keeping a high critical temperature difference at which larger cracks would start propagating [38]. This is important for enduring multiple thermal shock cycles.

Furthermore, the evolution of the flexural strength for the investigated sample types was analysed in dependence on the number of thermal shocks and is shown in Fig. 9a. The corresponding strength losses are shown in Table 6. The observed decreases in strength were also evalutated using boxplots where relevant changes corresponds to a non-overlapping of boxes within each sample series.

For A1 (tabular alumina) and A3 (AZT), the general evolution of the box plots is very similar reflecting a decreasing trend of the flexural strength: For both compositions the comparison of 1 TS and 5 TS show a not-relevant decrease of the flexural strength because of the strong overlapping of the boxes. The comparison of the sintered state (0 TS) to 1 TS yielded only a small overlapping in the case of A1 (tabular alumina) or the boxes just did not overlap in the case of A3 (AZT) indicating a certain loss in strength for both composition. Followingly, the decrease in strength in the comparison between 0 TS and 5 TS is also relevant for both compositions.

These data show that both materials were exposed to damaging effects on the microstructure, which is expected due to thermal stresses following thermal shock cycles [36]. But they exhibit only a gradual loss in strength with increasing number of thermal shocks. Hence, the loss per additional thermal shock (up to 5 times) decreases as the change in flexural strength from 1 TS to 5 TS (covering four consecutive thermal shocks) is not evaluated as relevant and less pronounced then the loss in strength after 1 TS. This effect is also seen in data of the relative loss of the flexural strength for A1 (tabular alumina) and A3 (AZT) presented in

Table 6. For A1 (tabular alumina), the relative strength loss after 1 TS related to 0 TS was practially equal (20.0 %) to the loss after 5 TS related to 1 TS (19.7 %). Regarding A3 (AZT), the loss in flexural strength after 1 TS related to 0 TS is evenly decreasing from 30.5 % to 23.2 % for 5 TS related to 1 TS. So for both materials, the relative strength loss after 1 TS in relation to the sintered state (0 TS) is in the same order of magnitude as the strength loss after 5 TS in relation to 1 TS, although the latter covers the influence of four thermal shock cycles.

For understanding this behaviour, the microstructure of the samples A1 (tabular alumina) and A3 (AZT) after one and five thermal shock tests was analysed by SEM (Fig. 10). Additonally, pore size distributions were registered by mercury intrusion porosimetry for each sample type after 1 TS and 5 TS to characterize the evolution of its microstructure during thermal shock load. The normed cumulative pore volume curves are shown in Figs. 11, 12 and 13 for the three sample types in comparision to the curves after sintering (0 TS). The 50th and 90th percentiles of the normed cumulative pore size curves are presented in Table 5.

Fig. 10 presents representative SEM images of the fractured surfaces of A1, A2 and A3 samples after 1 TS and 5 TS. It can be seen that the rapid heating and cooling of the samples during thermal shock tests led to the formation of cracks (marked with arrows in Fig. 10) due to the introduction of thermal stresses within the structure. This is also reflected by the evolution of the pore size distributions. For A1 (tabular alumina) the general appearance of the normed cumulative pore volume curve remains the same with increasing number of thermal shocks (Fig. 11). However, the fraction of pores smaller than d_{90} decreased for the distributions after 1 TS and 5 TS, which is considered as the opening of small pores due to the intended energy dissipation of propagating cracks. The pore size distributions of A3 (AZT) (Fig. 13) keep their general appearance independently of the number of applied thermal

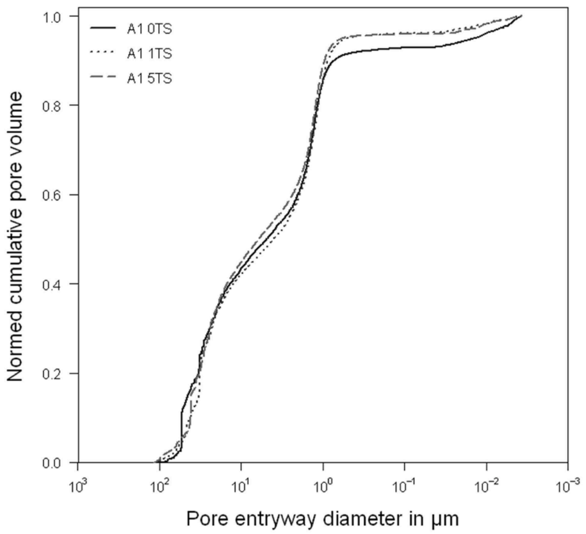

Fig. 11. Normed cumulative pore size distribution of A1 (tabular alumina) after sintering (0TS), one (1TS) and five (5TS) thermal shocks measured by MIP.

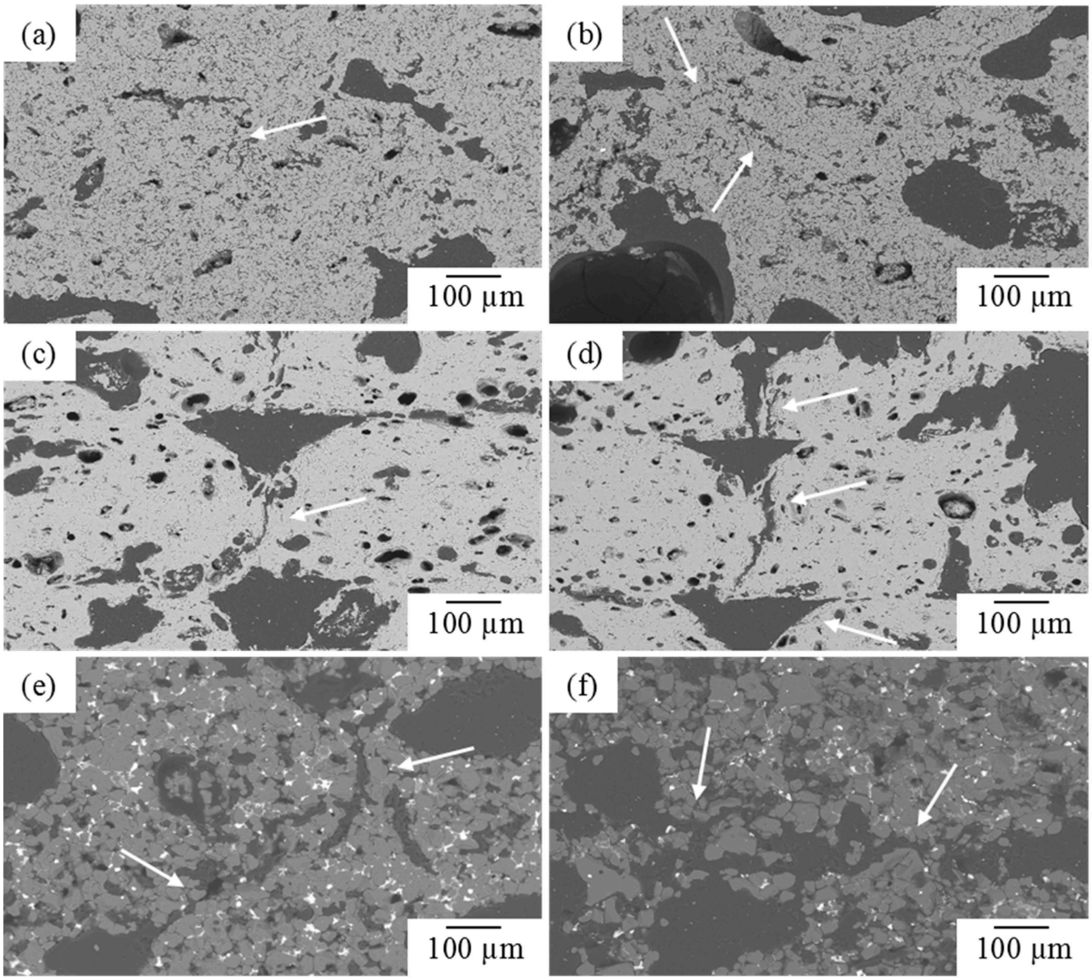

Fig. 10. SEM images (BSE mode) of the (a, b) A1, (c, d) A2 and (e, f) A3 sample cross-section after (a, c, e) one and (b, d, f) five thermal shocks (embedded and polished comparable cross-sections of representative samples from each thermal shock cycle); large cracks marked by arrows.

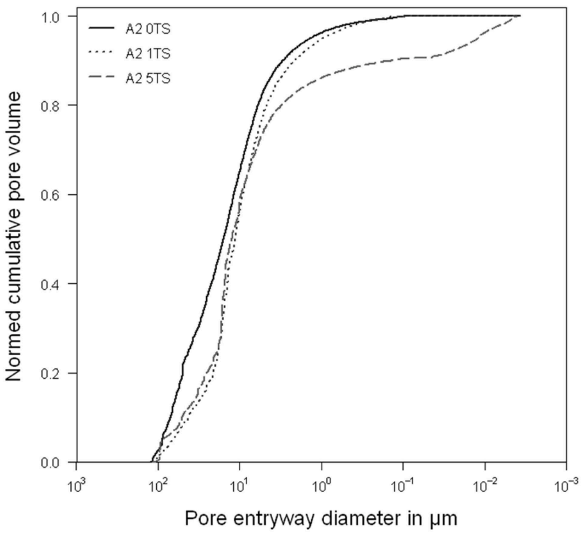

Fig. 12. Normed cumulative pore size distribution of A2 (reactive alumina) sintering (0TS), one (1TS) and five (5TS) thermal shocks measured by MIP.

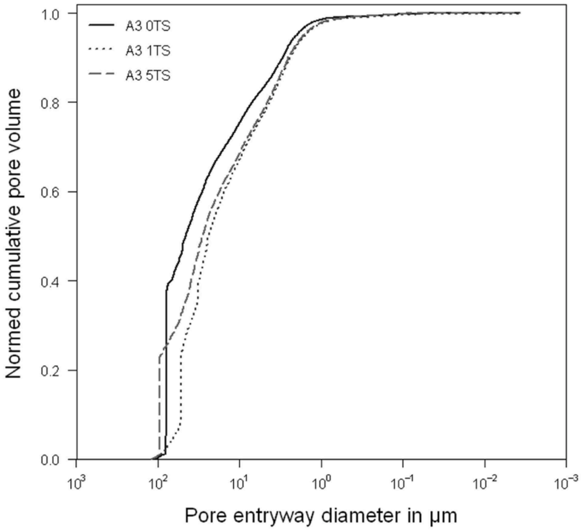

Fig. 13. Normed cumulative pore size distribution of A3 (AZT) after sintering (0TS), one (1TS) and five (5TS) thermal shocks measured by MIP.

shocks. For all three curves, an almost vertical section of the normed cumulative pore volume curve is observed during the initial filling of the open pores in the sample with mercury. It is considered that the applied mercury pressure causes a compression during the measurement exceeding locally the mechanical strength. As A3 (AZT) has the lowest strength level of the investigated compositions, a breaking of the microcracked material and a filling of suddenly created cavities in the material is likely and results in the steep increase of the curve. Thus, the actual d_{50} and d_{90} values should be lower compared to the measured data. Again, the specific percentile values were considered as an estimate, but the resulting order of magnitude and observed trends were regarded as a reliable result. The changes in the pore size distribution seem to occur in the middle-sized fraction of the pore size distribution, as shown by the decrease of the pore size of the 50th percentile (d_{50}). This decrease corresponds to an increase of smaller pores and is presumably related to the formation of cracks. The special microstructure of the material was considered as responsible for this effect due to the presence of multiple phases, which are on the same length scale as the value of d_{50} (see Fig. 4c, grain sizes up to 40 µm) causing stresses and thus further damaging cracks already formed during sintering.

Furthermore, EBSD investigations were perforemd for A3 (AZT) after five thermal shocks to evaluate possible changes of the initially present multiple phases. Fig. 14 shows an exemplary phase distribution of composition A3 (AZT) after 5 TS. Next to corundum as main phase, monoclinic ZrO_2 is visible originating from the microstructure after the initial sintering (see Fig. 7). Additonally, sodium containing phases can be observed, which correspond to the group of β-Al_2O_3-phases and to the group of Na-Al-titanate-phases. Due to the high number of phases in these groups with similar electron backscatter pattern, a reliable phase identification was not possible. Sodium is introduced into the material system by the used tabular alumina raw material. It contains approx. 0.4 wt % Na_2O as common impurity from the production process (Bayer process). Na_2O reacts with the initially formed Al_2TiO_5 and TiO_2 (Fig. 7) during the repeated input of thermal energy during the five thermal shock cycles at 1100 °C. The decomposition of Al_2TiO_5 at temperatures <1280 °C to Al_2O_3 and TiO_2 [11] might contribute to the reaction with Na_2O. Previous studies [39] observed similar reactions of within AZT materials and the formation of Na-Al-titanates using tabular alumina as raw material. Nonetheless, the formation of new phases under thermal load could provide a regeneration potential. The effect of the formation of these phases on the long-term stability of material A3 (AZT) will be investigated in future studies.

According to Hasselman [40], elastic disconinuities such as micropores, initial cracks or phase boundaries act as crack inhibitor, since the elastic energy for further crack propagation is dissipated when a crack reaches these discontinuities. These processes are considered to be responsible for the strength evolution of the sample types A1 (tabular alumina) and A3 (AZT). Due to intergranular porosity (Fig. 4), macroporosity (Fig. 5) and additonally for A3 (AZT) the presence of secondary phases with initial microcracks (Figs. 7 and 14), the crack propagation behaviour is controlled and no catastrophic crack growth takes place for the applied temperature difference. The evolution of the microstructure during the first thermal shock seemed to enhance the capacity of the material to endure thermal stresses because of the resulting microdamages, which permit the dissipation of elasting energy during the up to five subsequent thermal shocks. This resulted in the only gradual strength loss after the first thermal shock for samples A1 (tabular alumina) and A3 (AZT).

The samples A2 (reactive alumina) exhibit a different behavior. Only the strength loss after 1 TS compared to the sintered state (0 TS) is not relevant as shown by the overlapping boxes for 0 TS and 1 TS in Fig. 9b. However, the following thermal shocks cause a relevant decrease in flexural strength as it is shown by the comparisons of the samples in the sintered state (0 TS) and after 5 TS as well as after 1 TS and after 5 TS, since the boxes do not overlapp.

Firstly, this can be explained by the microstructure of the material A2 (reactive alumina). The samples have a certain potential to withstand a thermal shock load as it is shown by the non-relevant difference between the strength in the sintered state (0 TS) and after 1 TS, which can be explained by the existing pores in the samples. But compared to the other materials, its comparably high densification with a low interparticle porosity (Fig. 4) did not arrest crack propagation as effective as in materials A1 (tabular alumina) and A3 (AZT). This resulted in an increased damage formation with each thermal shock in contrast to the other two sample types. The changes in the pore size distribution reinforce this observation. Fig. 12 shows that the value for d_{50} is reduced after 1 TS which is considered as a formation of new cavities which correspond to cracks. After 5 TS the fraction of fine cavities has strongly increased as the value for d_{90} decreased to 0.1 µm which is considered as the formation of numerous fine cracks in an attrition-like process. This explains the strongly reduced flexural strength after 5 TS.

This behaviour corresponds to fine-grained dense ceramic components with a brittle fracture characterisitc [36]. Due to the regular, relatively homogeneous microstructure without initial pores of such ceramic materials, the potential to dissipate elastic energy from thermal

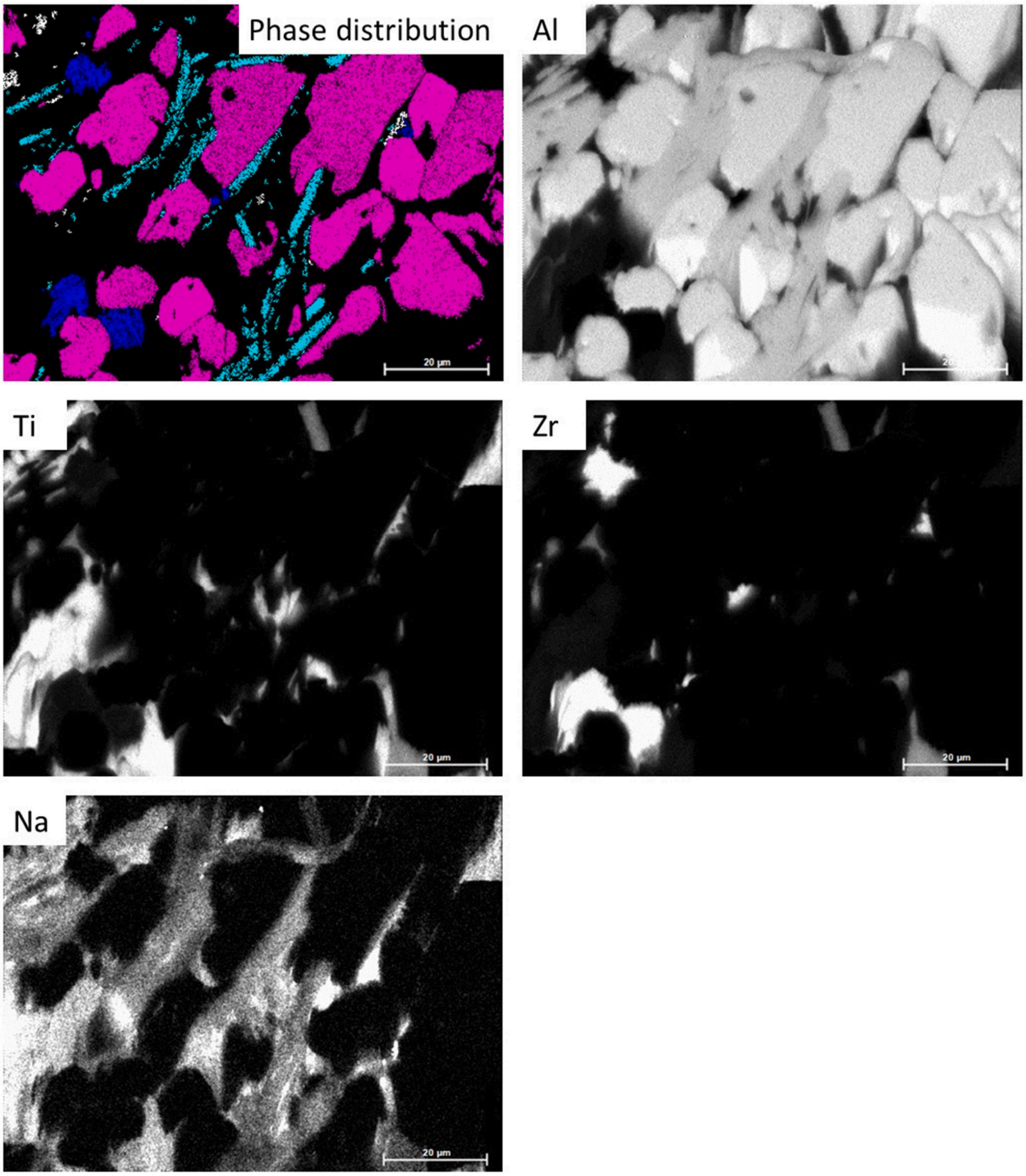

Fig. 14. EBSD and EDX analysis for A3 (AZT) after 5 thermal shocks, phase distribution: pink – corundum, blue – monoclinic ZrO_2, white – Na-Al-titanate, turquoise – β-Al_2O_3.

stresses is strongly reduced. In the case of A2 (reactive alumina), the pore channel structure and pores from the debinding process are available to arrest cracks in that way, that a catastrophic crack growth is prevented and the samples survive the thermal shock series. However, the thermal shocks were accompanied with a high strength loss of 62.6 % between 0 TS and 5 TS (Table 6).

Secondly, the material specific mechanical properties resulting from the microstructure are relevant, which is expressed by thermal shock parameters. For refractory materials, the thermal shock-damage-resistance-parameter R'''' and the thermal-shock-resistance-paramter R_{st} are of particular importance (Eqs. (2) and 3) [38]. The material's behaviour regarding propagation and arresting of small cracks is described by R'''', which is specifically interesting for the material systems investigated in this study as they are based on fine-grained raw materials. According to Larson et al. [38], a relatively low tensile strength σ_t, combined with a high Young's modulus E and a high fracture energy γ results in high values of R'''' and minimizes the crack growth of small cracks during thermal shock. The parameter R_{st} is relevant for the behaviour of large cracks under thermal shock, which can be considered secodarily due to the presence of channel structures from the printing process and macropores from the debinding step corresponding to comparably large heterogeneities for the present sample geometry. Here, a relatively low Young's modulus E is relevant next to a low coefficient of thermal expansion α and a high fracture energy γ to achieve high values of R_{st} and thus, to increase the critical temperature difference for crack propagation of long cracks in the material.

$$R'''' = \frac{\gamma E}{\sigma_t^2} \tag{2}$$

$$R_{st} = \left(\frac{\gamma}{\alpha^2 E}\right)^{1/2} \tag{3}$$

In order to evaluate the observed thermal shock behaviour, the presented thermal shock parameters are taken into account for the

Table 7
Ratios of the mean values of Young's modulus and flexural strength² (E/σ^2) according to R'''' for A1 (tabular alumina) and A2 (reactive alumina).

	E_0/σ^2 in Pa^{-1}	
	A1 (tabular alumina)	A2 (reactive alumina)
0 TS	$4.34 \cdot 10^{-5}$	$2.02 \cdot 10^{-5}$
1 TS	$5.76 \cdot 10^{-5}$	$1.99 \cdot 10^{-5}$
5 TS	$9.60 \cdot 10^{-5}$	$13.01 \cdot 10^{-5}$

materials A1 (tabular alumina) and A2 (reactive alumina). They can be compared since both consist of corundum. Due to their identical chemistry and phase composition (apart from technical impurities), the fracture energy and the coefficient of thermal expansion were considered as comparable for the solid material within the scale of the material strands resulting from the additive manufacturing process. Furthermore, the flexural strength σ was used as parameter to approximate the strength behaviour of the materials. Hence, these properties as well as the ratio between the Young's modulus and the square of the flexural strength (E/σ^2) according to R'''' are to be discussed.

Table 7 shows the ratio E/σ^2 for A1 (tabular alumina) and A2 (reactive alumina) in the sintered state (0 TS) and after 1 TS and 5 TS. The data show that the ratios are growing during the series of five thermal shocks for both material types. However, the starting level in the sintered state (0 TS) is for A1 (tabular alumina) approximately twice as high as for A2 (reactive alumina) and after 1 TS approximately threefold compared to A2 (reactive alumina). In contrast to this, the ratio remains practically constant for A2 (reactive alumina) during the first thermal shock (1 TS). After five thermal shocks the ratio of A2 (reactive alumina) is approximately 1/3 higher than for A1 (reactive alumina). So, A2 (reactive alumina) has low values for the ratio E/σ^2 at the beginning of the thermal shock series going along with low values for R''''. This corresponds well to the reduced potential to endure consecutive thermal shock loads as shown by the strength evolution in Fig. 9a presenting a relevent strength loss after 5 TS compared to the sintered state (0 TS) and 1 TS. In contrast, the initial level of E_0/σ^2 is higher for A1 (tabular alumina) corresponding to a better initial suitability for thermal shock loads compared to A2 (reactive alumina). So only a gradual strength loss occurred for A1 (tabular alumina).

Additonally, the magnitude of E has to be regarded in relation to R_{st} where comparably low levels of the elastic modulus are desired [38] to obtain a high critical temperature difference to be endured by the material. Since A2 (reactive alumina) has the highest level of E of the investigated sample compositions, it is assumed that the initial values for E and their relation to σ are less favorable for A2 (reactive alumina) compared to A1 (tabular alumina). However, the micorstructural changes of A2 (reactive alumina) during the thermal shock series change this relation towards an improved range shown by the rising ratio of E/σ^2 (Table 7). It was considered, that the high strength loss after 5TS combined with an only gradual decrease of the elastic modulus (Fig. 8) resulting the increasing ratio of E/σ^2 is related to the formation of fine cracks as reflected by the measured pore size distribution. The strong reduction of the value of d_{90} (Fig. 12 and Table 5) shows a strong increase of fine cavities throughout the whole material and corresponded probably to homogeneously distributed defects in the microstructure. Hence, the material A2 (reactive alumina) has limited thermal shock performance in the present state and a limited applicability. However, it could provide a suitable thermal shock behaviour with an adapted microstructure. Future studies will focus on this approach to reach a suitable strength evolution directly in the sintered state.

Furthermore, the obtained ratios of E/σ^2 can be compared to data from the literature. Larson et al. [38] investigated commercially availabe alumina refractories and measured both flexural strength and Young's modulus. For alumina samples with a purity of 99 % values for E/σ^2 of $19.0 \cdot 10^{-5}$ Pa^{-1} and $29.0 \cdot 10^{-5}$ Pa^{-1} can be calculated. They are in the same order of magnitude as the obtained levels of E/σ^2 after 5 TS, which is remarkable as the commercially available refractories have normally a different microstructure due to the use of coarse-grained raw material fractions. This enhances the suitability for thermal shock applications compared to fine-grained ceramics and explains the slightly higher ratios of E/σ^2. However, the similarity of the ratios of E/σ^2 of the samples of the present study (A1, A2) after 5 TS and the literature data for commercially available alumina refractories underlines the abilities of additive manufacturing processes to tailor the microstructure for thermal shock applications independently of the maximum raw material grain size [25,27].

Finally, the observed behaviour of the investigated materials under thermal shock load can be summarized as follows: The three investigated materials systems showed strong differences in their elastic modulus level with A2 > A1 > A3 because of the different microstructural character. The Young's modulus remained practically constant for A1 (tabular alumina) as well as A2 (reactive alumina) and showed only a minor decrease, which remained cloes to the sintered state. This observation was done for up to five thermal shocks going along with a preserving of the initial potential to arrest small cracks and the initial critical temperature difference of the material. For A3, the decreasing trend of Young's modulus was more pronounced compared to the other two compositions. But the loss in elastic modulus per additional thermal shock decreased, which was also favorable for repeated thermal shock load up to five cycles.

Regarding the evolution of the flexural strength of the investigated samples, it can be noted that a gradual decrease of the flexural strength was observed for A1 (tabular alumina) and A3 (AZT) with increasing number of thermal shocks. However, this gradual loss per thermal shock decreased for up to five thermal shocks underlining the high potential of A1 and A3 to withstand repeated thermal shocks. A2 (reactive alumina) has initially a limited potential to withstand thermal stresses due to its comparably high density. However, the evolution of its ratio E/σ^2 with increasing thermal shock cycles up to five times suggested an improved thermal shock behaviour with an adapted microstructure.

3.3. *Tests in ammonia combustion atmosphere*

Ammonia combustion tests were conducted in a heated slot burner as described in Section 2.3. Fig. 15 shows the setup in the cold state and a representative sample during exposure (gas-phase temperature at the sample location > 1500 °C, exposure time 1 h). All samples survived the test without macroscopic damages. The sample integrity remained intact (mass change < 0.3 %).

After the test, the samples were broken, prepared and their polished cross-sections analyzed regarding changes in chemical composition and phase alteration. Fig. 16 presents exemplary EBSD measurements for all samples. The image quality (IQ) pictures reveal only crystalline phases. A1 (tabular alumina) and A2 (reactive alumina) consisted only of corundum equal to the sintered state. A3 (AZT) shows again a multiphase microstructure, which also contain the initial phases (see also Fig. 7). Hence, it can be stated that no relevant changes of the material occurred during the applied test under ammonia combustion atmosphere. Consequently, all investigated sample compositions evinced a favorable chemical resistance for the application in ammonia combustion burners. Long term tests will be done in future investigations.

3.4. *Manufacturing of model components*

Sheet-gyroid-based model structures ($29.8 \times 29.8 \times 28.3$ mm³ without supplier tubes) were printed using the material system A1 (tabular alumina) to demonstrate the transferability of the manufacturing process to application near geometries. The component consisted of a sheet-gyroid structure surrounded by a casing and equipped with connectors for two separate gas inlets as it is required for non-premixed combustion processes. Fig. 17 shows exemplarily a printed, a debinded and a sintered component. The intended geometry was

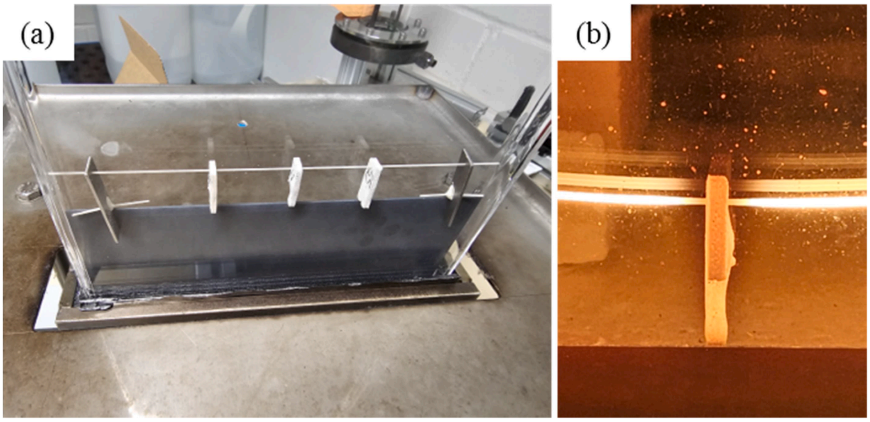

Fig. 15. Samples in the slot burner (a) and in the hot state during ammonia combustion test (b).

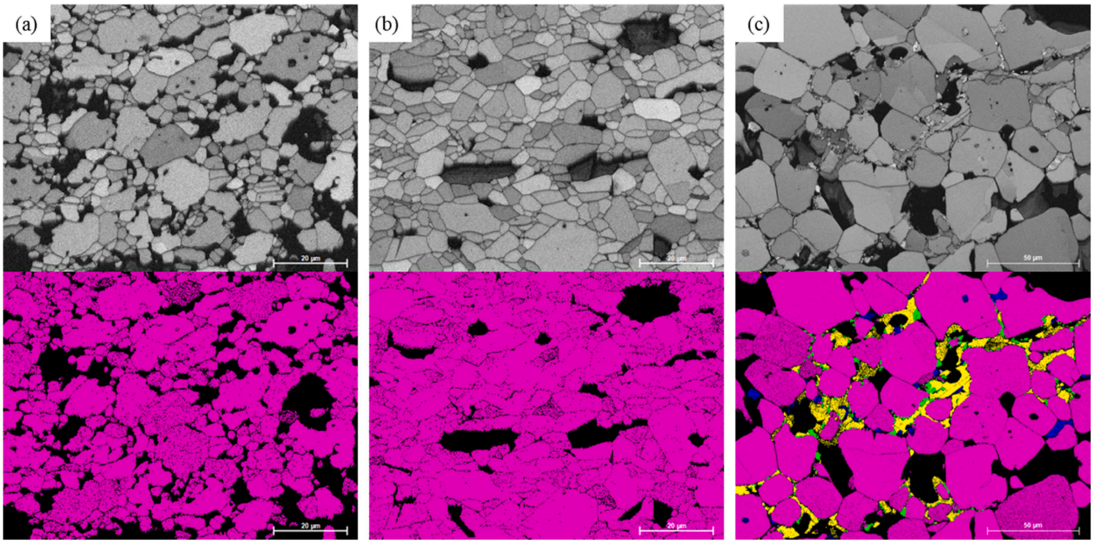

Fig. 16. EBSD analysis for (a) A1, (b) A2 and (c) A3; top: IQ image, bottom: phase distribution: pink – corundum, blue – monoclinic ZrO_2, green – TiO_2, yellow – Al_2TiO_5, purple – $ZrTiO_4$.

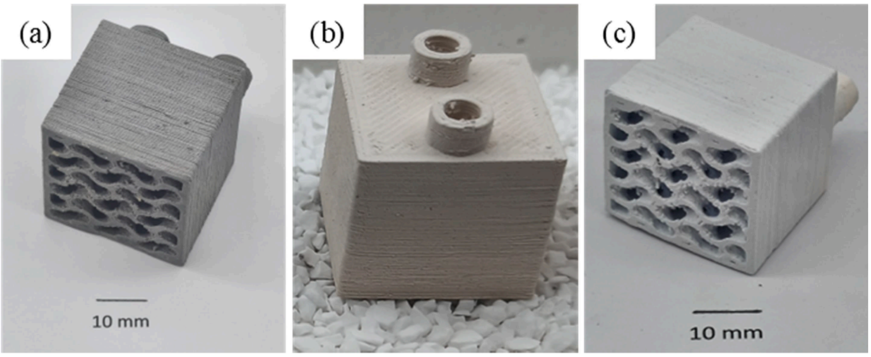

Fig. 17. Model component for burner applications, a) printed state, b) debinded state, c) sintered state.

successfully realized.

To evaluate the internal structure of the components, CT-scans were performed and 2D CT-images of an exemplary component with a voxel size of (23.17 µm)^3 after reconstruction are presented in Fig. 18. The intended channel structure of the components is intact. In the bulk material, a fine porous structure is detectable, which is related to the manufacturing via the printing process and the removal of the binder materials during the thermal treatments. The mechanical properties of these components depending on printing parameters, component size and load direction will be investigated in future studies.

4. Conclusions

This study focused on the fabrication of alumina-based model samples by fused granulate fabrication for the application in burner components for ammonia combustion. Three material systems were

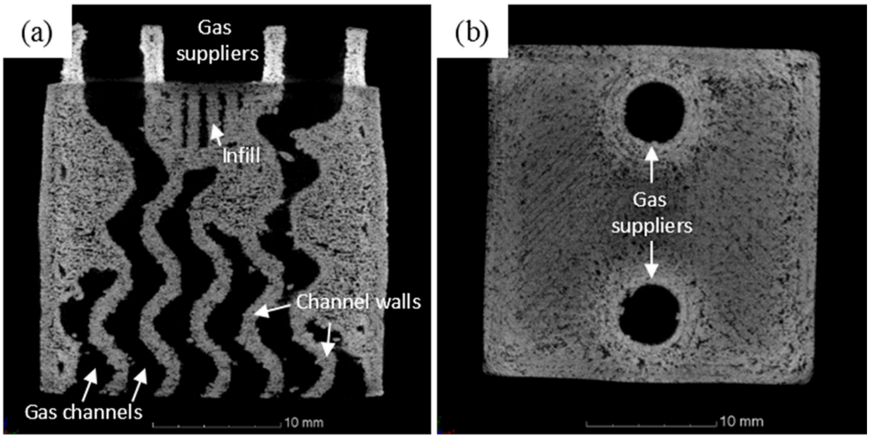

Fig. 18. 2D-CT images of the sintered model component (voxel size 23.17 × 23.17 × 23.17 μm^3), a) vertical cross-section, b) horizontal cross-section near the connectors.

investigated: Two pure alumina systems differing by their initial grain size (A1 – tabular alumina, A2 – reactive alumina) as well as alumina with MgO-stabilzed ZrO_2 and TiO_2 additions (2.5 wt % each, A3 – AZT). For all material compositions, the previously investigated binder system [24,27,28] developed for a purely thermal debinding process was transferred and the intended prismatic samples were successfully manufactured.

The obtained mechanical properties differed for the three compositions in the Young's modulus and the flexural strength. While the highest values were determined for A2 (reactive alumina) due to a higher sintering degree and lower interparticle porosity (flexural strength of 210.35 MPa and Young's modulus of 102.14 GPa), A3 (AZT) showed considerably lower values for the Young's modulus (31.29 GPa) and the flexural strength (7.99 GPa) compared to A1 (tabular alumina) and A2 (reactive alumina). These observations were mainly attributed to the presence of secondary and newly formed phases exhibiting differences in the thermal expansion coefficients and hence causing the formation of microcracks in the AZT (A3) microstructure.

Furthermore, thermal shock investigations showed that A1 (tabular alumina) exhibited the best suitability for repeated thermal shocks up to five cycles due to the initial microstructural state, which provided sufficient cracks, pores to limit crack propagation. This resulted in only a slow, gradual loss in Young's modulus (up to 8.6 %) and strength (up to 35.7 %) with increasing number of thermal shocks. A3 (AZT) showed losses in Young's modulus and strength up to 58.6 % and 46.6 %, respectively. Here, the additional positive effect of the formation of new phases under thermal load occurred. A1 (tabular alumina) offered the higher overall strength level for handling purposes. Nonetheless, A3 (AZT) constitutes a promising alternative for large scale components if a medium strength level is required. A2 (reactive alumina) was characterized by a pronounced loss in strength due to thermal shock load. However, the microstructural evolution with increasing number of thermal shock cycles improved the ability of the A2 material (reactive alumina) to withstand thermal shocks.

The analysis of ratios of the Young's modulus related to the squared flexural strength (E/σ^2) of the pure alumina materials A1 (tabular) and A2 (reactive alumina) exhibited ratios in the same order of magnitude as for coare-grained alumina. This observation underlined the possibility to tailor the microstructure of ceramic materials for thermal shock applications independently of the maximum particle size.

Moreover, tests in ammonia combustion atomosphere at approx. 1500 °C for 1 h showed no phase alterations of the three investigated materials, which suggests a favorable chemical resistance for the application as burner material. Finally, model components with application-near geometries were successfully realized. Future strudies will focus on long-term tests under ammonia combustion atmosphere, the use fine-grained raw materials for AZT, the manufacturing of graded structures with different porosities for tailored thermal shock behaviour and the investigation of the mechanical properties of application-near geometries.

CRediT authorship contribution statement

Benjamin Bock-Seefeld: Writing – review & editing, Writing – original draft, Visualization, Validation, Software, Methodology, Investigation, Formal analysis, Data curation. **Daniel Kretzler:** Writing – review & editing, Validation, Methodology, Investigation, Data curation. **Claudia Heuer:** Writing – review & editing, Validation, Investigation. **Marc Neumann:** Writing – review & editing, Visualization, Validation, Formal analysis. **Jana Hubálková:** Writing – review & editing, Visualization, Validation, Methodology, Investigation, Data curation. **Björn Stelzner:** Writing – review & editing, Validation, Methodology, Investigation, Conceptualization. **Oliver T. Stein:** Writing – review & editing, Supervision, Resources, Project administration, Funding acquisition, Conceptualization. **Dimosthenis Trimis:** Writing – review & editing, Supervision, Resources, Project administration, Funding acquisition, Conceptualization. **Christos G. Aneziris:** Writing – review & editing, Supervision, Resources, Project administration, Funding acquisition, Conceptualization. **Nora Brachhold:** Writing – review & editing, Writing – original draft, Visualization, Validation, Supervision, Software, Methodology, Investigation, Formal analysis, Data curation, Conceptualization.

Declaration of competing interest

The authors declare that they have no known competing financial interests or personal relationships that could have appeared to influence the work reported in this paper.

Acknowledgement

The authors would like to thank the German Research Foundation (DFG) for the financial support of this study within the framework of the Priority Program "SPP 2419 HyCAM", subproject 10 (Project-ID 523876164). Furthermore, the authors would like to acknowledge all participants of the Institute of Ceramics, Refractories and Composite Materials and the Karlsruhe Institute of Technology KIT, who assisted the investigations of the present study.

References

[1] Refractories Handbook, The Technical Association of Refractories of Japan, 1998. Tokyo, JapanISBN 9-925133-01-2.

[2] C.B. Carter, M.G. Norton, Ceramic Materials Science and Engineering, Springer Science+Business Media, LLC, New York, USA, 2007. ISBN 0-387-46270-8.

[3] S. Chalia, M. Naagara, P. Thakur, A. Thakur, S.N. Sridhara, An overview of ceramic materials and their composites in porous media burner applications, Ceram. Int. 47 (2021) 10426–10441.

[4] N. Gerlach, C.G. Aneziris, F. Lange, H. Grote, Coars-grained ceramic heat shields made by pressure slip casting, Refractories Worldforum 7 (2015) 101–104.

[5] N. Gerlach, C.G. Aneziris, D. Trimis, E. Reusse, Refractories in innovative heating technologies for the glass industry, Refractories Manual (2008) 80–82.

[6] O. Pickenäcker, K. Pickenäcker, K. Wawrzinek, D. Trimis, W.E.C. Pritzkow, C. Müller, P. Goedtke, U. Papenburg, J. Adler, G. Standke, H. Heymer, W. Tauscher, F. Jansen, Novel ceramic components for high-temperature applications in porous medium burner technology, II, in: Keramische Zeitschrift, 53, 2001, pp. 780–787.

[7] C. Wei, L. Gremillard, Towards the prediction of hydrothermal ageing of 3Y-TZP bioceramics from processing parameters, Acta Mater. 144 (2018) 245–256.

[8] X. Liang, Y. Li, J. Liu, S. Sang, Y. Chen, B. Wenli, C.G. Aneziris, Fabrication of SiC reticulated porous ceramics with multi-layered struts for porous media combustion, Ceram. Int. 42 (2016) 13091–13097.

[9] C.G. Aneziris, W. Schärfl, B. Ullrich, Microstructure evaluation of Al_2O_3 ceramics with Mg-PSZ- and TiO_2 -additions, J. Eur. Ceram. Soc. 27 (2007) 3191–3199.

[10] J. Fruhstorfer, S. Möhmel, M. Thalheim, G. Schmidt, C.G. Aneziris, Microstructure and strength of fused high alumina materials with 2.5 wt% zirconia and 2.5 wt% titania additions for refractory applications, Ceram. Int. 41 (2015) 10644–10653.

[11] B. Freudenberg, A. Mocellin, Aluminum titanate formation by solid-state reaction of fine Al_20_3 and $Ti0_2$ powders, J. Am. Ceram. Soc. 70 (1987) 33–38.

[12] C.G. Aneziris, S. Dudczig, N. Gerlach, H. Berek, D. Veres, Thermal shock performance of fine grained Al_2O_3 ceramics with TiO_2 and ZrO_2 additions for refractory applications, Adv. Eng. Mater. 12 (2010) 478–485.

[13] R.D. Bagley, I.B. Cutler, D.L. Johnson, Effect of TiO_2 on initial sintering of Al_2O_3, J. Am. Ceram. Soc. 53 (1970) 136–141.

[14] A. Valera-Medina, M.O. Vigueras-Zuniga, H. Shi, S. Mashruk, M. Alnajideen, A. Alnasif, J. Davies, Y. Wang, X. Zhu, W. Yang, Y.B. Cheng, Ammonia combustion in furnaces: a review, Int. J. Hydrogen. Energy 49 (2024) 1597–1618.

[15] A. Valera-Medina, H. Xiao, M. Owen-Jones, W.I.F. David, P...J.. Bowen, Ammonia for power, Prog. Energy Combust. Sci. 69 (2018) 63–102.

[16] A. Hayakawa, T. Goto, R. Mimoto, Y. Arakawa, T. Kudo, H. Kobayashi, Laminar burning velocity and Markstein length of ammonia/air premixed flames at various pressures, Fuel 159 (2015) 98–106.

[17] H. Kobayashi, A. Hayakawa, K.K.A. Somarathne, E.C. Okafor, Science and technology of ammonia combustion, Proc. Combust. Inst. 37 (2019) 109–133.

[18] G. Vignat, T. Zirwes, E. Boigné, M. Ihme, Experimental demonstration of a two-stage porous media burner for low-emission ammonia combustion, Proc. Combust. Inst. 40 (2024) 105491.

[19] G. Vignat, T. Zirwes, E.R. Toro, K. Younes, E. Boigné, P. Muhunthan, L. Simitz, D. Trimis, M. Ihme, Experimental and numerical investigation of flame stabilization and pollutant formation in matrix stabilized ammonia-hydrogen combustion, Combust. Flame 250 (2023) 112642.

[20] D. Kretzler, R. Puri, B. Stelzner, T. Zirwes, F.P. Hagen, O.T. Stein, D. Trimis, Experimental and numerical investigation of non-premixed ammonia flames stabilized on a heated slot burner, Proc. Combust. Inst. 41 (2025) 105854.

[21] D. Kretzler, R. Puri, B. Stelzner, T. Zirwes, G. Vignat, F. Hagen, O.T. Stein, M. Ihme, D. Trimis, Non-premixed ammonia combustion in porous media to promote thermal cracking of NH3: a low-emission burner concept, 2026, Available at SSRN: https://ssrn.com/abstract=6294678 or doi:10.2139/ssrn.6294678.

[22] S. Wood, A.T. Harris, Porous for lean-burn application, Prog. Energy Combust. Sci. 34 (2008) 667–684.

[23] W. Kollenberg, Additive Fertigung Keramischer Komponenten: Grundlagen und Anwendungen, Vulkan Verlag, Essen, Germany, 2020. ISBN 978-3-8027-3114-3.

[24] C. Heuer, B. Bock-Seefeld, P. Kaiser, C. Weigelt, P. Malczyk, N. Brachhold, D. Trimis, C.G.C. Aneziris, 3D printing of alumina components via Fused Granulate Fabrication technology and solvent-free debinding of highly filled feedstocks comprising (LD)-polyethylene and cellulose, Ceram. Int. 51 (2025) 58287–58296.

[25] C. Heuer, R. Soth, F. Kerber, C. Wöhrmeyer, C. Parr, C.G. Aneziris, 3D-Manufactured thermal shock resistant zirconia based macrostructures for use as functional components in metallurgical applications, Proceed. Unitecr (2025) 348–351.

[26] C. Aneziris, S. Yaroshevskyi, P. Malczyk, Filaments for the thermoplastic 3D production of ceramic components, metallic components or components based on metal-ceramic composites or material composites, German patent WO2023186645A1, 2023.

[27] S. Yaroshevskyi, P. Malczyk, C. Weigelt, J. Hubalkova, S. Dudczig, U. Lohse, C. G. Aneziris, Fused filament fabrication of thermal-shock-resistant fine-grained refractories for steel-casting applications, Ceramics 6 (2023) 475–491.

[28] P. Malczyk, F. Kerber, P. Kaiser, B. Bock-Seefeld, C. Heuer, C.G. Aneziris, Development of powder bed pre-debinding techniques for the manufacturing process of 3D-printed multi-material parts made of polyethylene-based ceramic, metal and metal–ceramic filaments, Ceram. Int. 52 (2026) 8803–8816.

[29] D.C. Montgomery, G.C. Runger, N.F. Hubele, Engineering Statistics, Wiley & Sons, New York, USA, 2007. ISBN 978-0-471-73557-1.

[30] O. Al-Ketan, R.K.A. Al-Rub, MSLattice: a free software for generating uniform and graded lattices based on triply periodic minimal surfaces, Mater. Design Process. Commun. 3 (2021) e205.

[31] A. Kebbede, J. Parai, A.H. Carim, Anisotropic grain growth in α-A_2O_3 with SiO_2 and TiO_2 additions, J. Am. Ceram. Soc. 83 (2000) 2845–2851.

[32] Y.-M. Kim, S.-H. Hong, D.-Y. Kim, Anisotropic abnormal grain growth in TiO_2/SiO_2-doped alumina, J. Am. Ceram. Soc. 83 (2000) 2809–2812.

[33] D.S. Horn, G.L. Messing, Anisotropic grain growth in TiO_2-doped alumina, Mater. Sci. Eng. 195 (1995) 169–178.

[34] J.S. Reed, Principles of Ceramic Processing, Wiley & Sons, New York, USA, 1995. ISBN 978-0-471-59721-6.

[35] D. Qin, Y. Li, S. Li, J. Li, C. Wei, Synthesis, microstructure and physical properties of aluminium titanate ceramics modified by multiple additives, J. Alloys. Compd. 1010 (2025) 177456.

[36] W.D. Callister, Materials Science and engineering: An introduction, Wiley & Sons, New York, USA, 2007. ISBN 978-0-471-73696-7.

[37] E. Brochen, J. Pötschke, C.G. Aneziris, C. G, Improved thermal stress resistance parameters considering temperature gradients for bricks in refractory linings, Int. J. Appl. Ceram. Soc. 11 (2014) 371–383.

[38] D.R. Larson, J.A. Coppola, D.P.H. Hasselman, R.C. Bradt, Fracture toughness and spalling behavior of high-Al_2O_3 refractories, J. Am. Soc. 57 (1974) 417–421.

[39] P. Gehre, C.G. Aneziris, M. Klinger, M. Schreiner, M. Neuroth, Influence of TiO_2 -and ZrO_2 -addition on the interaction of alumina castable with molten coal and gasifier slag, Fuel 150 (2015) 252–260.

[40] D.H.P. Hasselman, Elastic energy at fracture and surface energy as design criteria for thermal shock, J. Am. Ceram. Soc. 46 (1963) 535–540.